

# INVERSION OF STRONG GROUND MOTION AND TELESEISMIC WAVEFORM DATA FOR THE FAULT RUPTURE HISTORY OF THE 1979 IMPERIAL VALLEY, CALIFORNIA, EARTHQUAKE

BY STEPHEN H. HARTZELL AND THOMAS H. HEATON

## ABSTRACT

A least-squares point-by-point inversion of strong ground motion and teleseismic body waves is used to infer the fault rupture history of the 1979 Imperial Valley, California, earthquake. The Imperial fault is represented by a plane embedded in a half-space where the elastic properties vary with depth. The inversion yields both the spatial and temporal variations in dislocation on the fault plane for both right-lateral strike-slip and normal dip-slip components of motion. Inversions are run for different fault dips and for both constant and variable rupture velocity models. Effects of different data sets are also investigated. Inversions are compared which use the strong ground motions alone, the teleseismic body waves alone, and simultaneously the strong ground motion and teleseismic records. The inversions are stabilized by adding both smoothing and positivity constraints.

The moment is estimated to be  $5.0 \times 10^{25}$  dyne-cm and the fault dip  $90^\circ \pm 5^\circ$ . Dislocation in the hypocentral region south of the United States-Mexican border is relatively small and almost dies out near the border. Dislocation then increases sharply north of the border to a maximum of about 2 m under Interstate 8. Dip-slip motion is minor compared to strike-slip motion and is concentrated in the sediments. The best-fitting constant rupture velocity is 80 per cent of the local shear-wave velocity. However, there is a suggestion that the rupture front accelerated from the hypocenter northward. The 1979 Imperial Valley earthquake can be characterized as a magnitude 5 earthquake at the hypocenter which then grew into or triggered a magnitude 6 earthquake north of the border.

## INTRODUCTION

The 15 October 1979 (23:16:54) Imperial Valley earthquake ( $M_L = 6.6$ ) provided a wealth of strong-motion records. Twenty-two records were obtained from the U.S. Geological Survey network in the Imperial Valley within an epicentral distance of 60 km (Brady *et al.*, 1980) and seven records were obtained from the northern Baja California strong-motion array (Brune *et al.*, 1982). The strong-motion records, together with the teleseismic recordings, make the 1979 Imperial Valley earthquake the best-instrumented, moderate-sized event to date, with the possible exception of the 1971 San Fernando earthquake. The complicated topographic and geologic setting of the San Fernando earthquake makes it difficult to study. In comparison, the structure of the Imperial Valley is relatively simple, consisting of a deep sedimentary basin with relatively flat-lying layers. Furthermore, a recent seismic refraction study of the area (Fuis *et al.*, 1982) yielded fairly detailed information on the  $P$ -wave velocity structure. Thus, recordings of the 1979 Imperial Valley earthquake provide us with a unique opportunity to construct detailed and physically realistic models of the rupture history and wave propagation for this earthquake. Failure to adequately model records from this earthquake would seriously undermine our confidence in the validity of previous modeling studies of earthquakes for which less data is available.

To date, the strong-motion data set has formed the basis of a number of studies.

Niazi (1982) determined acceleration directions using the horizontal ground motions across a differential array at El Centro (station locations indicated by DIF in Figure 7). This array consists of five digital accelerometers positioned on a north-south line 210 m long. From these data, Niazi inferred that the rupture propagated northwestward from the epicenter in Mexico. Niazi further estimated an average rupture velocity of 2.7 km/sec during the first 6 sec of faulting. Spudich and Cranswick (1982) have also analyzed the El Centro differential array data. They calculated apparent velocities of particular phases by cross-correlating records. Their work implies an average rupture velocity of 2.5 km/sec at depth, but also suggests that the rupture velocity was lower during the first few seconds of faulting and that the rupture accelerated as it moved to the north. Their analysis also suggests that large high-frequency vertical accelerations (0.6 to 1.74 *g*) recorded on several strong-motion records near El Centro are due to *P* waves originating from the vicinity of the Imperial fault where it crosses Interstate 8 and at a depth of approximately 8 km. Archuleta (1982) proposed the alternative interpretation that the large vertical accelerations are a surface-reflected *PP* phase originating further to the south near Bonds Corner at a depth of about 4 km. By examining polarization diagrams of particle velocity for stations near the trace of the fault, Archuleta (1982) estimated an average rupture velocity of 2.5 to 2.6 km/sec.

Three previous studies have used the strong-motion data to estimate the distribution of slip for the 1979 earthquake: Hartzell and Helmberger (1982), Olson and Apsel (1982), and Le Bras (1983). Hartzell and Helmberger (1982) used forward modeling to deduce the slip distribution. Their model is characterized by an average rupture velocity of 2.5 to 2.7 km/sec (0.8 to 0.9 times the basement shear-wave velocity). The slip is predominantly below a depth of 5 km, north of the hypocenter and south of the El Centro area. Two regions of noticeably larger slip were suggested, particularly one located under Interstate 8, which is held to be responsible for the large vertical accelerations recorded near El Centro. They estimated the moment from strong-motion records to be  $5.0 \times 10^{25}$  dyne-cm, which was shown to be consistent with the amplitudes of teleseismic shear waves. Olson and Apsel (1982) used a least-squares inversion. They parameterized the problem by dividing the Imperial fault plane into sections, 2 with depth and 10 along the strike of the fault. Each section, or subfault, is allowed to rupture during five separate time intervals, each separated by 0.75 sec. Their slip distribution is significantly smoother than the model of Hartzell and Helmberger (1982). The major differences in the two models may be due to the different parameterizations of the problem. Hartzell and Helmberger (1982) used a constant rupture velocity, with fixed timing, requiring that the waveforms be explained by spatial variations in slip. Olson and Apsel (1982) set the problem up with more capacity for temporal variation and less spatial variation in slip. They obtained a trend in dynamic slip which implied a horizontal rupture velocity between 4.0 and 5.0 km/sec, which is greater than the local shear-wave velocity. This slip, although more smoothly distributed than the patch of large dislocation in the Hartzell and Helmberger (1982) model, is located in the same place and may be a manifestation of the same phenomenon. The present study has a more balanced trade-off between spatial and temporal model parameters than these previous two studies. Olson and Apsel (1982) obtained a moment of  $9.1 \times 10^{25}$  dyne-cm.

Le Bras (1983) used an inversion scheme which minimizes a cross-correlation error function between the synthetic waveform and the data. A constant rupture velocity is used, but the mechanism (strike, dip, and rake) of each subfault is allowed

to vary somewhat about a pure right-lateral, strike-slip,  $90^\circ$ -dipping fault. He found that the fits to the strong-motion records are improved by allowing the strike, dip, and rake to vary by  $\pm 10^\circ$ . As in the previous studies, the Le Bras (1983) model is characterized by an average rupture velocity of about 2.5 km/sec, with most of the slip below 5 km and north of the hypocenter but south of the El Centro area. He estimated the moment to be  $5.0 \times 10^{25}$  dyne-cm.

In this paper, unlike the previous studies, we model both the teleseismic body waves and the local strong-motion records. The teleseismic data are included in an attempt to add additional constraints on the rupture process. We also wish to address a basic question: What details of the rupture history can be deduced from (1) teleseismic data alone, (2) near-source data alone, and (3) the combined teleseismic and near-source data sets? This is an important question, since good local instrument coverage is rare and most earthquake source studies must depend on teleseismic data alone. Heaton (1982) recently demonstrated the difficulties involved in modeling teleseismic body waves and strong ground motions simultaneously with a forward modeling approach and showed the inconsistencies which can develop between models obtained by forward modeling of limited data sets. Thus, one of the objectives of this paper is to explore the similarities and differences of inversion models based on different data sets. The data are modeled by using a constrained, stabilized, least-squares inversion technique. The problem is parameterized to yield the best-fitting (in a least-squares sense) dislocation on a spatially and temporally discretized fault.

#### FORWARD PROBLEM

Before pursuing the inverse problem, several forward models of the teleseismic body waves were run. These calculations are done to investigate the dip of the Imperial fault and to see what contributions individual phases make to the teleseismic waveforms. Hartzell and Helmberger (1982) obtained a model of the distribution of dislocation for the 1979 earthquake by forward modeling of just the strong-motion data. It is also of interest to see how well this model predicts the teleseismic body waves.

Figure 1 shows the seismic velocity structures used throughout this study to compute strong ground motion (dashed curves) and teleseismic synthetics (solid curves). The local  $P$ -wave velocity structure (Table 1) is based closely on the refraction results of Fuis *et al.* (1982) and is an average velocity structure for profile 6NNW-13SSE of that study, which runs approximately down the axis of the Imperial Valley. The  $S$ -wave velocities are obtained by assuming (1) a Poisson solid ( $\alpha = \sqrt{3} \beta$ ) below a depth of 5 km and (2) linearly increasing Poisson's ratio for depths less than 5 km such that  $\alpha = 2.37 \beta$  at the free surface. The structure used to compute the teleseismic waveforms (Table 1) consists of three layers over a half-space and approximates the gradient structure used in the near-source region. This simplified structure greatly reduces the computational effort required to model teleseismic body waves from a finite fault. Use of the layered structure to compute the teleseismic body waves is justified by their longer period and the steep teleseismic take-off angles. The computation of teleseismic body-wave synthetics for a three-dimensional finite fault is done by a Green's function summation technique. Heaton (1982) gives a full explanation of the method. The teleseismic synthetics in this paper include the responses of all rays with up to two internal reflections in the layered stack. All conversions between phases occurring at the free surface are included as well as the more important internal conversions. The amplitudes of

rays having a greater number of internal reflections are much smaller and can be omitted. Point source responses for sources embedded within the gradient structure (approximated by many layers) were computed using a Haskell propagator matrix technique and compared favorably with responses computed using the generalized ray technique and assuming the simplified velocity model. The Haskell matrix method is not used in the rest of this study because the analysis requires the separation of the responses of down-going ( $P$ ,  $S$ ) and up-going ( $pP$ ,  $sP$ ) phases, a modification not yet implemented in the Haskell method.

The teleseismic, long-period  $P$  and  $SH$  waves predicted by the Hartzell and Helmberger (1982) model 9WM are shown in Figures 2 and 3, respectively. All WWSSN  $P$  and  $SH$  waveforms of acceptable quality between  $30^\circ$  and  $90^\circ$  are shown. In both figures the synthetic is the second, lighter trace. The amplitude in microns is given for each synthetic assuming a moment of  $5.0 \times 10^{25}$  dyne-cm. This moment was obtained by Hartzell and Helmberger in their study of the strong-motion records. The waveforms and amplitudes of the  $P$  waves are fairly well-matched. The

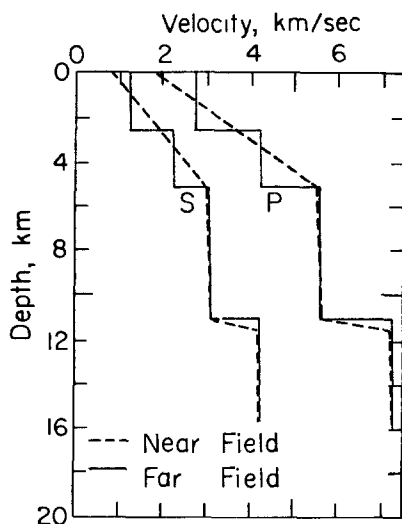


FIG. 1. Near-field velocity structure used to compute strong-motion synthetics and far-field velocity structure used to compute teleseismic body-wave synthetics.

$SH$  waveforms are well modeled except for the two nodal stations MAL and SJG, which appear to be contaminated by noise. Perhaps the most obvious difference is the much longer, complicated waveforms of the observed  $P$  waves, lasting for over 1 min. The waveform complexities arrive much too late to be explained by source effects, and may be due to structural complexities in the source and receiver regions. We will mention the long  $P$ -wave durations again when we discuss the record section length to be used in the inversion. In general, the Hartzell and Helmberger (1982) near-source model does a good job of predicting the teleseismic body-wave amplitudes, and a fair job of modeling the waveforms.

Hartzell and Helmberger (1982) and Olson and Apsel (1982) both assumed a vertical dip for the Imperial fault. However, Archuleta (1982) used epicentral distributions and results of seismic refraction studies (Fuis *et al.*, 1982) to argue in favor of a  $75^\circ$  NE dip. Well-located epicenters (horizontal error less than 2.5 km) along the Imperial fault tend to cluster on the east side of the fault (Johnson, 1979). Upon first inspection, this pattern suggests that the Imperial fault dips to the east

at about  $75^\circ$ . However, Johnson (1979) argued convincingly that many of these earthquakes are not actually occurring on the Imperial fault plane. It appears that the seismicity is actually occurring along a collection of north-south-trending planes aligned along the northwest-southeast-trending Imperial fault. The resulting pattern is one in which seismicity is distributed to the northeast of the observed fault trace, thus creating the illusion of a dipping fault. The dip of the Imperial fault is explored further in Figures 4 and 5. These two figures compare long-period  $P$  and  $SH$  synthetics, respectively, for different dips at four stations widely spaced in

TABLE 1  
CRUSTAL STRUCTURES

Depth (km)	$\alpha$ (km/sec)	$\beta$ (km/sec)	$\rho$ (gm/cm <sup>3</sup> )
Near-Source Crustal Structure*			
0.0	1.9	0.8	1.80
5.0	5.5	3.0	2.55
11.0	5.6	3.14	2.70
11.5	7.2	4.16	2.80
Teleseismic Crustal Structure†			
0.0	2.75	1.25	2.0
2.5	4.25	2.25	2.25
5.0	5.55	3.1	2.65
11.0	7.2	4.2	2.8

\* Elastic parameters vary linearly between the horizons.

† Elastic parameters constant between the horizons.

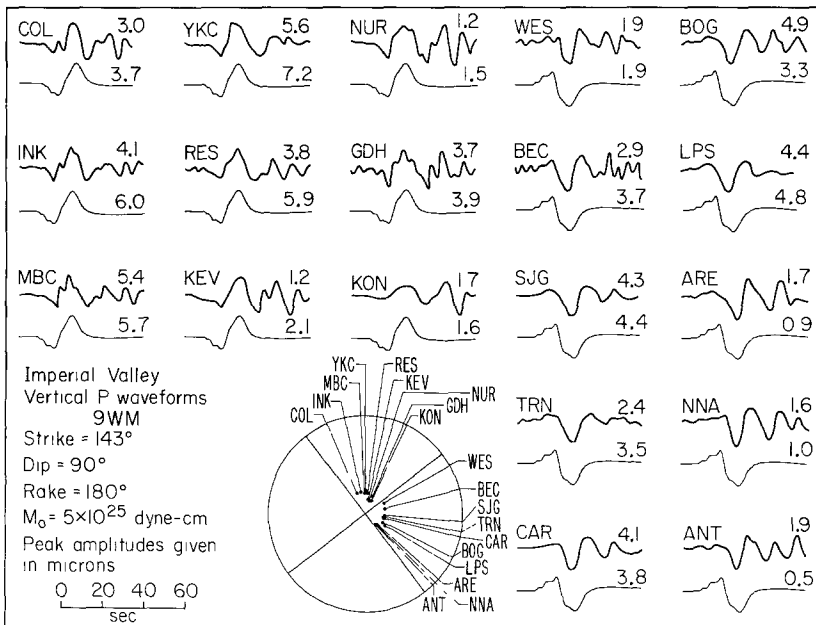


FIG. 2. Comparison of observed (top trace) and computed (bottom trace) teleseismic, long-period, vertical  $P$  waves for model 9WM of Hartzell and Helmberger (1982). Amplitudes of synthetics are for a moment of  $5.0 \times 10^{25}$  dyne-cm.

azimuth. The 9WM model of Hartzell and Helmberger (1982) is used. Synthetics are shown for dips of  $80^\circ$  west to  $75^\circ$  east in  $5^\circ$  increments. From the amplitudes and waveforms in Figures 4 and 5, it is difficult to pick one dip which explains the data better than any other. The  $P$  waves are somewhat more diagnostic than the  $SH$  waves. Station ANT is near nodal for  $P$  as are other stations to the south. These stations rule out dips of  $75^\circ$  east and shallower. We conclude that any dip in the range of  $90^\circ$  plus or minus  $5^\circ$  does an equally good job of fitting the data. There may also be small-scale variations in the strike, dip, and rake along the fault as suggested by Le Bras (1983).

To determine the contributions of individual teleseismic phases to the total waveform, the long- and short-period  $P$ -wave synthetics for model 9WM are decomposed in Figure 6. Each record is shown broken down into the contributions of  $P$ ,  $pP$ ,  $sP$ , and the combined response of the remaining phases. One interesting feature of the ray decomposition is the fact that the  $P$ ,  $pP$ , and  $sP$  phases are each smaller than the combined response of all other phases, particularly at longer

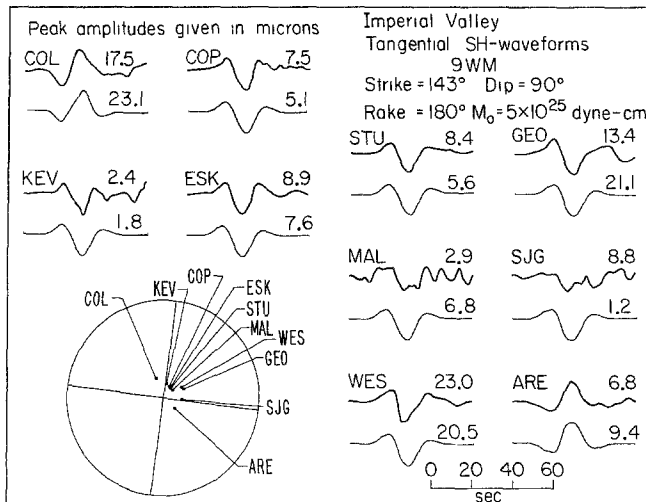


FIG. 3. Comparison of observed (top trace) and computed (bottom trace) teleseismic, long-period tangential  $SH$  waves for model 9WM of Hartzell and Helmberger (1982). Amplitudes of synthetics are for a moment of  $5.0 \times 10^{25}$  dyne-cm

periods. This result is explained when one considers the gradient-like nature of the earth structure assumed. Since there is such a large velocity variation within the sediments, the ray which reflects off the free surface should not be expected to be significantly larger than rays reflecting internally in the sediments. Thus, the  $P$ ,  $pP$ , and  $sP$  phases are each similar in amplitude or smaller than the collective response of all the reflected and converted phases within the sediments. Waves reflected from a velocity gradient are smoothly distributed in time. Thus, reflection off of a gradient is analogous to low-pass filtering. Therefore, the energy reflected from a gradient has a long-period spectrum. This explains why the combined response of all other phases is more prominent in the long-period records, compared to the phases  $P$ ,  $pP$ , and  $sP$ , than in the short-period records.

#### DATA SET AND PREPROCESSING

*Strong-motion data.* The surface trace of the Imperial fault and the strong-motion stations of interest to this study are shown in Figure 7. The epicenters of both the

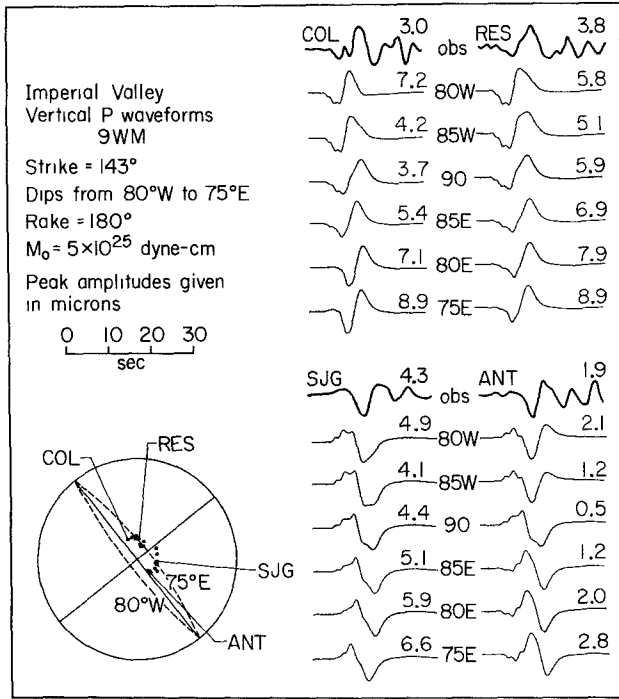


FIG. 4. Variation in long-period P waveforms with fault dip for model 9WM of Hartzell and Helmberger (1982). Amplitudes of synthetics are for a moment of  $5.0 \times 10^{25}$  dyne-cm.

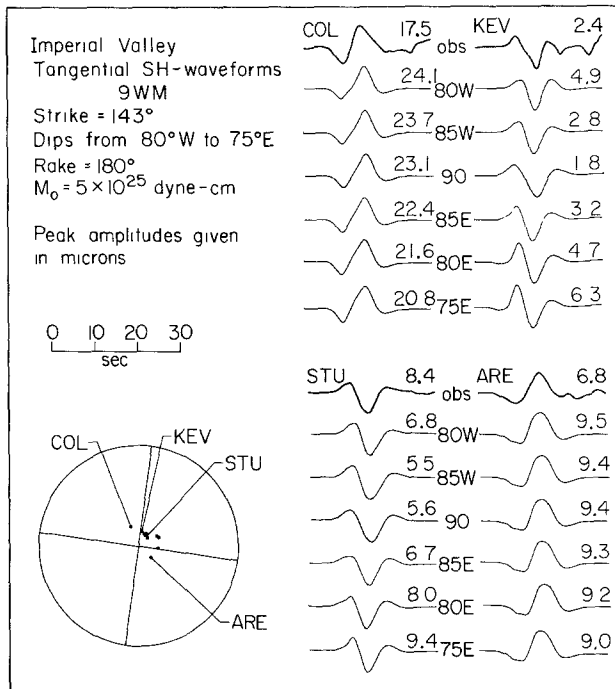


FIG. 5. Variation in long-period SH waveforms with fault dip for model 9WM of Hartzell and Helmberger (1982). Amplitudes of synthetics are for a moment of  $5.0 \times 10^{25}$  dyne-cm.

1979 and 1940 Imperial Valley earthquakes are indicated by stars (Chavez *et al.*, 1982). The instruments forming the El Centro strong-motion array are labeled numbers 1 through 13. The two horizontal components from the following 12 stations are used in the inversion: from the El Centro array numbers, 3, 4, 5, 7, 8, 10, and 11, the El Centro differential array station, Calexico, Meloland, Holtville, and Bonds Corner.

The vertical components of strong ground motion are not used because of incomplete knowledge of the seismic velocity structure. The  $P$ -wave velocities are fairly well-known from refraction surveys. However, the  $S$ -wave velocities have been deduced from the  $P$ -wave velocities assuming a particular distribution of Poisson's ratio. Poisson's ratio controls the  $S$ -minus- $P$  time. Therefore, if we have misjudged Poisson's ratio, we cannot simultaneously match the correct arrival time of the  $P$  and  $S$  waves. Hartzell and HelMBERGER (1982) noted this problem and

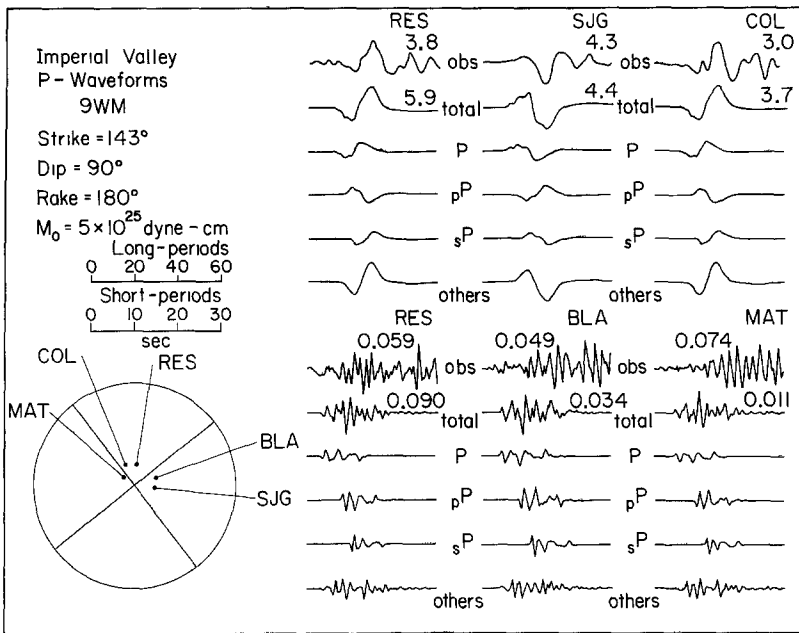


FIG. 6. Decomposition by phase ( $P$ ,  $pP$ ,  $sP$ , and all other phases combined) of selected long- and short-period, teleseismic, vertical  $P$  waves for model 9WM of Hartzell and HelMBERGER (1982).

observed that the vertical synthetics match the observations better if they are shifted in time a small amount relative to the horizontal components. To avoid this problem, we have chosen to model only the horizontal components, which are predominantly shear-wave energy.

The Green's functions used to calculate the strong-motion synthetics are computed with the DWFE (Discrete Wavenumber/Finite Element) code of Olson (1982), which is similar to the finite-difference method of Alekseev and Mikhailenko (1979, 1980). The advantage of this code is that it can easily handle linear gradients in material properties, such as encountered in the upper 5 km of the Imperial Valley (Figure 1). The Green's functions include all theoretical arrivals within the specified time interval and are valid in the frequency band from 0.0 to 2.0 Hz.

Since a linear, least-squares inversion is to be used, care must be taken to use only linear operations when processing the data. We wish to model the velocity

records, rather than the displacements, because the velocities preserve more of the high-frequency information. Traditionally, strong-motion records have been processed with a parabolic baseline correction and band-pass filtered with an Ormsby filter (Trifunac, 1971; Trifunac *et al.*, 1973); however, the baseline correction procedure is a nonlinear operation. We have applied an alternative straightforward processing procedure. The digitized accelerograms (U.S. Geological Survey phase I data) are firstly linearly interpolated to a uniform time step of 0.01 sec. The instrument correction is applied and the records are integrated to velocity by a trapezoidal rule. The velocity records are then band-pass filtered from 0.1 to 1.0 Hz with a Butterworth filter (Oppenheim and Schafer, 1975). To preserve zero phase shift, the filter is applied twice, once in the forward direction and once in the reverse direction. Finally the records are linearly interpolated to a uniform time step of 0.2

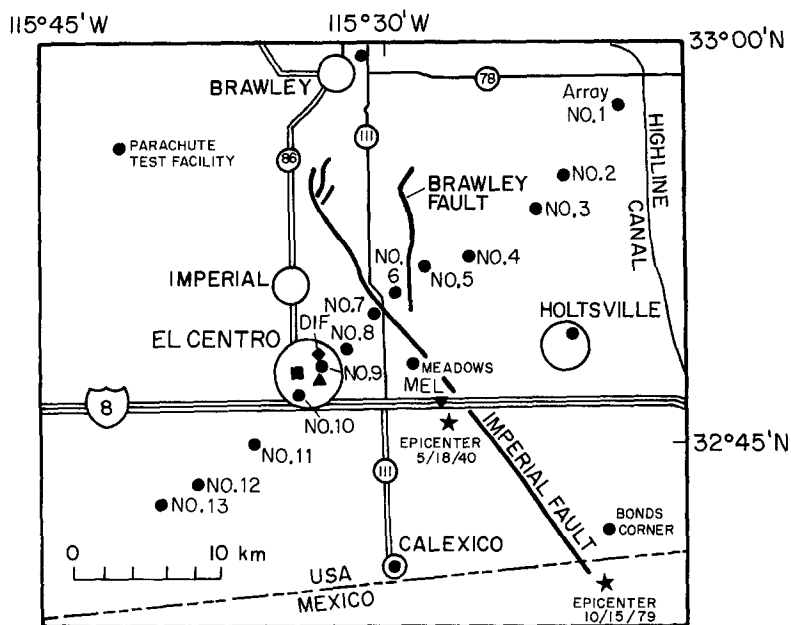


FIG. 7 Local map of the Imperial Valley showing the surface traces of the Imperial and Brawley faults and the locations of strong-motion instruments.

sec. The synthetics are band-pass filtered in an identical manner and linearly interpolated to the same time step of 0.2 sec.

In the least-squares inversion, it is necessary to specify the relative timing between the observed and synthetic records. This correlation is accomplished by relating both records back to the origin time of the earthquake. To relate the observed records with the origin time, the trigger time of the instrument is required. Of the 12 strong-motion stations used in this study, seven have readable trigger times. The trigger times for the remaining five stations are estimated in the following manner. Initial trigger times are estimated based on the station's distance from the epicenter and the trigger times of nearby instruments. A preliminary inversion of the data is done using a constant rupture velocity of  $0.8\beta$  (technique to be discussed in the following section). The observed and synthetic records for this inversion are then compared. Of the five stations without trigger times, the synthetics for four of them

fit the observations significantly better with a small time shift. The time shifts are no greater than 1 sec. All the following inversions of the strong-motion records then use these new estimates of the trigger times.

Another important parameters to be considered in the inversion problem is the record length to be used. Two different lengths were tried for the strong-motion data, 17.5 and 35 sec. For most of the stations, the strong shaking is over in 10 sec or less, thus initially it may not be clear if a long record section need be used. However, the important consideration is not the amplitude of the records, but the time required for the rupture front to propagate down the entire length of the model fault plus the time required for the slowest phase of interest to travel to the most distant station used in the inversion. If shorter record sections are used, the dislocation on the more remote sections of the fault will be less well constrained. When 17.5 sec of record is used, artificially large dislocations are obtained on the ends of the fault. Therefore, a record length of 35 sec is used.

*Teleseismic data.* The teleseismic data set consists of 19 long-period, vertical  $P$  waves, 10 long-period, tangential  $SH$  waves, and 7 short-period, vertical  $P$  waves. The station distribution can be seen in Figures 2 and 3. Small signal amplitudes and high noise levels make stations to the west and southwest unusable. The long-period records are band-pass filtered from 0.0166 to 1.0 Hz. The short-period records are band-pass filtered from 0.075 to 1.0 Hz. A zero phase shift Butterworth filter is used in all cases. The filtering is done to remove long-period drift and high-frequency noise. The teleseismic records are sampled at a uniform time step of 0.25 sec for the long periods and 0.1 sec for the short periods.

The teleseismic synthetics are calculated in the same manner as discussed previously for the forward problem. The same source-time function is used for the teleseismic synthetics as for the strong-motion synthetics. Attenuation is entered with the Futterman  $Q$  operator (Futterman, 1962) with constant  $t^* = T/Q$  (Carpenter, 1966), where  $T$  is the ray travel time and  $Q$  is the average seismic quality factor along the ray. We have used the following values for  $t^*$ : 4.0 for long-period  $SH$ , 1.0 for long-period  $P$ , and 0.7 for short-period  $P$ . The synthetics are band-pass filtered with the same filter as used on the data and interpolated to the same uniform time step.

Great care must be taken with the teleseismic records to obtain accurate enough timing for the inversion. An error in timing of 1 sec corresponds to an error in location of the rupture front on the fault of 2.5 km for a rupture moving at 80 per cent of the shear-wave velocity. To obtain this kind of accuracy or better, it is necessary to pick arrival times from short-period records. However, the first arrivals on the short-period  $P$ -wave records have a very emergent character (see Figure 8). It is not possible to pick the first arrival on these records to the required accuracy. To solve this problem, we calculate the expected first  $P$ -wave arrival time for the Imperial Valley earthquake from the observed local origin time and from station residuals derived for the 1968 Borrego Mountain earthquake. The first arrival time for the Imperial Valley earthquake,  $T_I$ , at a particular station is given by

$$T_I = 0_I + (T_B - 0_B) + (\Delta_I - \Delta_B) \frac{dT}{d\Delta} + (d_B + d_I)\eta, \quad (1)$$

where  $0_I$ , is the origin time of Imperial Valley,  $T_B - 0_B$  is the travel time for Borrego Mountain,  $\Delta_I - \Delta_B$  is the difference in station distance for Imperial Valley and Borrego Mountain,  $dT/d\Delta$  is the  $P$ -wave ray parameter (based on Jeffreys-Bullen

earth model),  $d_B - d_I$  is the difference in hypocentral depths for Imperial Valley and Borrego Mountain, and  $\eta$  is the vertical slowness =  $[1/\alpha^2 - (dT/d\Delta)^2]^{1/2}$ . Table 2 shows the details of the timing calculation. The Borrego Mountain earthquake is used because of its proximity to the Imperial Valley earthquake and because it has an impulsive first arrival. The first arrival times for Borrego Mountain,  $T_B$ , are taken from the ISC catalog. Errors in  $T_I$  are estimated to be  $\pm 1/2$  sec for the long-period records and  $\pm 1/4$  sec for the short-period records. The short-period  $P$  waves in Figure 8 are aligned using the calculated first arrival times (indicated by the leftmost vertical line). It would be very difficult to pick these times from only an examination of the records. Accordingly, the ISC picks for this event have large errors.

Record length is also an important consideration for the teleseismic records. A rupture initiating at the hypocenter 5 km south of the international border and propagating the full length of the observed ground breakage is over in about 17 sec.

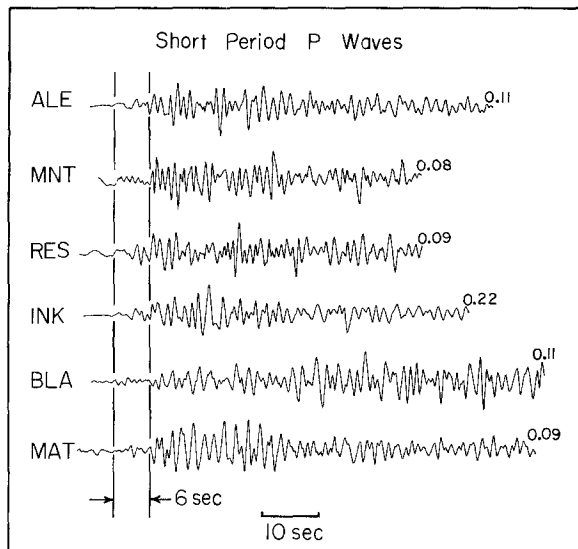


FIG. 8. Teleseismic, short-period, vertical  $P$  waves. First vertical line is the initial  $P$ -wave arrival time. Second vertical line indicates arrival time of significant energy 6 sec later. Peak amplitudes given in microns.

Yet from Figure 8, we see that the short-period  $P$  waves have durations of over 1 min. Peak amplitudes often do not occur until late in the records. The same complexities are seen in the long-period  $P$  waves. Figure 9 compares the long-period  $P$  waves recorded at BOG for the Imperial Valley earthquake and the 26 April 1981 ( $M_L = 5.6$ ) Westmorland earthquake, which also occurred in the Imperial Valley, 36 km north of El Centro. Both events exhibit long, complicated  $P$  waveforms. The fact that this complexity is seen for large and small earthquakes alike in the Imperial Valley strongly suggests that it is not a source effect. Our teleseismic Green's functions, which include the responses of reflected and transmitted rays for flat-lying layers, cannot explain the long-record durations in Figures 8 and 9. We do not have a definitive explanation for the later arriving energy. However, the observations suggest trapping of energy either within the valley by lateral heterogeneities, nonplanar interfaces, and/or dipping structures or by similar mechanisms

near the receiver. Since our model does not include these structures, we use only the initial, primary portions of the  $P$ -wave records in the inversion. The record lengths used are: 30 sec for long-period  $P$  waves, 35 sec for long-period  $SH$  waves,

TABLE 2  
TELESEISMIC ARRIVAL TIMES

Station	$T_B$ (min sec)	$T_B - 0_B$ (sec)	$\Delta_B$ (km)	$\Delta_I$ (km)	$\frac{dT}{d\Delta}$ (sec/km)	$(\Delta_I - \Delta_B) \frac{dT}{d\Delta}$ (sec)	$\eta$ (sec/km)	$(d_B - d_I)\eta$ (sec)	$T_I$ (min sec)
NNA	38:56.0	596.9	6504.28	6407.28	0.0645	-6.26	0.154	-0.62	26:44.5
ANT	40:26	686.9	7939.58	7843.01	0.0555	-5.36	0.157	-0.63	28:15.4
ARE	39:43.8	644.7	7252.29	7155.15	0.059	-5.73	0.156	-0.62	27:32.8
WES	36:06.5	427.4	4028.33	3991.82	0.077	-2.81	0.148	-0.59	23:58.5
COL	36:11.8	432.7	4129.1	4214.57	0.076	6.50	0.148	-0.59	24:13.1
GDH	37:52.9	533.8	5528.19	5553.88	0.068	1.75	0.152	-0.61	25:49.4
NUR	41:17.0	737.9	9035.42	9070.39	0.0485	1.70	0.159	-0.64	29:13.5
KEY	40:34.1	695.0	8218.67	8262.85	0.0535	2.36	0.158	-0.63	28:31.2
KON	40:55.5	716.4	8590.13	8614.57	0.0515	1.26	0.159	-0.64	28:51.5
BEC	37:01.0	481.9	4770.28	4712.31	0.0725	-4.20	0.150	-0.60	24:51.6
SJG	37:31.7	512.6	5233.33	5152.61	0.0705	-6.02	0.151	-0.60	25:20.5
TRN	38:28.4	569.3	6096.81	6011.49	0.066	-5.63	0.153	-0.61	26:17.6
CAR	37:58.0	538.9	5602.88	5514.55	0.0685	-6.05	0.152	-0.61	25:46.7
LPS	35:19.0	379.9	3434.82	3338.65	0.080	-7.7	0.146	-0.58	23:06.1
BOG	37:45.0	525.9	5380.55	5285.75	0.070	-6.64	0.151	-0.60	25:33.2
MAT	41:19	737.9	9109.18	9206.39	0.047	4.57	0.160	-0.64	29:18.3
BLA	35:03.5	364.4	3263.18	3211.89	0.080	-4.10	0.146	-0.58	22:54.2
MBC	37:02.3	483.2	4799.68	4863.41	0.072	4.59	0.150	-0.60	25:01.7
YKC	35:02	362.9	3261.03	3321.58	0.080	4.76	0.146	-0.58	23:01.6
RES	36:58.4	479.3	4766.69	4817.84	0.072	3.68	0.158	-0.63	24:56.8
MNT	35:50	410.9	3859.49	3831.88	0.0785	-2.17	0.147	-0.59	23:42.6
ALE	38:13.8	554.7	5864.50	5916.14	0.067	3.46	0.153	-0.61	26:12.0
FCC	35:05.2	366.1	3283.81	3311.96	0.080	2.25	0.146	-0.58	23:02.3

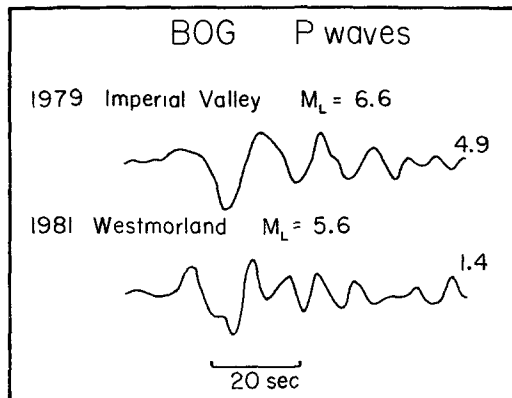


FIG. 9. Comparison of long-period, vertical  $P$  waves at BOG for 1979 Imperial Valley and 1981 Westmorland earthquakes. Peak amplitudes given in microns.

and 20 sec for short-period  $P$  waves. The  $SH$  waves are simple and the full duration of the waveforms is used.

#### INVERSION METHOD

We represent the rupture surface with a plane. This fault plane is divided into subfaults as shown in Figure 10. The basic approach is the same used by Trifunac

(1974) although many of the restrictions on model and structure parameters have been relaxed. Figure 10 is a side view of the Imperial fault from the west where the plunge axis runs down the dip of the fault. The locations of the El Centro array, Interstate 8, and the international border are indicated with arrows (refer to Figure 7). The fault is divided into 56 subfaults, all 3 km long and with the four depth intervals: 0 to 2.5 km, 2.5 to 5.0 km, 5.0 to 7.5 km, and 7.5 to 10.5 km. Synthetic ground motions are calculated for both a right-lateral, strike-slip dislocation and a normal (east-side down) dislocation of constant amplitude over each of the subfaults. Each of these calculations is repeated for every strong motion and teleseismic station in the inversion. The same Green's function summation and interpolation method is used as employed by Heaton (1982) and Hartzell and Helmberger (1982). We assume the epicenter of Chavez *et al.* (1982), approximately 5 km south of the border. The hypocenter is at a depth of 10.5 km, located in the bottom right-hand corner of subfault 48 in Figure 10. A rupture front propagates from the hypocenter at a constant fraction of the local shear-wave velocity. For a medium with no changes in shear-wave velocity, the rupture front would describe a circle of growing radius. For a medium with changing seismic velocities, such as the Imperial Valley (see Figure 1), the rupture front slows as it enters lower velocity material and no

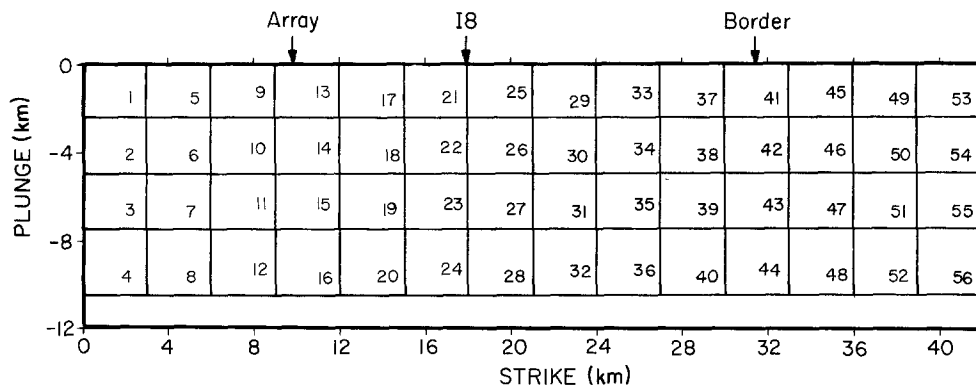


FIG. 10 Plane of the Imperial fault showing the 56 subfaults used in the inversion modeling of the strong-motion and teleseismic records. North is to the left and the hypocenter is in the bottom right-hand corner of subfault 48.

longer describes a circle. Ray tracing is used to define the position of the rupture front at any given point in time. Thus, the rupture front in our models is not circular [see Archuleta (1982), Figure 13, for an example of this calculation]. Although the velocity structure used to calculate the teleseismic synthetics is a simplified version of the structure used in the near-field (Figure 1), the advance of the rupture front is constrained to be the same as in the near-field calculations. Thus, the timing is consistent between the teleseismic and strong-motion synthetics. The dislocation time history at any point on the fault is assumed to be the time integral of a triangle with a 0.2-sec rise and a 0.5-sec fall, for a total rise time of 0.7 sec.

The observed and synthetic records form an overdetermined system of linear equations,

$$Ax \cong b, \quad (2)$$

where  $A$  is the matrix of synthetics,  $b$  is the data vector, and  $x$  is the solution vector of the subfault dislocation weights. This system of linear equations is shown

schematically in Figure 11. Each column of  $A$  is composed of the synthetics, strung end to end, for a particular subfault and a particular mechanism (either strike-slip or normal) for all the stations in the inversion. Similarly,  $b$  is formed by stringing all the observation records end to end. Thus, each time point on each record is explicitly included in the inversion. The number of columns of  $A$  depends on the number of elements in  $x$ . The elements of  $x$  are the amounts of strike-slip and dip-slip dislocations to be applied to each subfault to fit the observations. Figures 12 and 13 show a few subfault synthetics for selected strong-motion and teleseismic

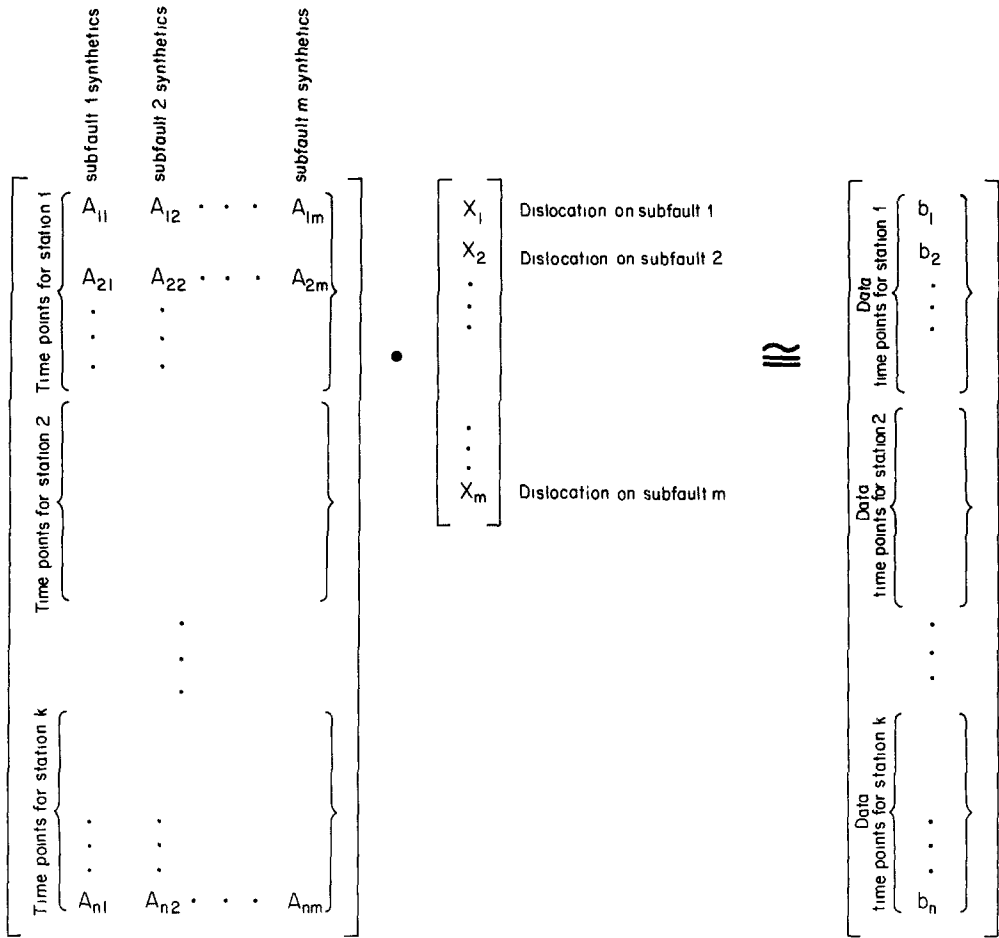


FIG. 11 Schematic of least-squares waveform inversion [equation (2)]; see text for detailed explanation.

stations. The number at the beginning of each trace is the subfault number (refer to Figure 10). Synthetics are shown for three vertical columns of subfaults; one near the northern end of the fault (subfaults 5 to 8), one near the middle (subfaults 29 to 32), and one near the southern end of the fault (subfaults 45 to 48). There are two synthetics for each subfault; the first is for a strike-slip mechanism and the second is for a dip-slip mechanism. The number at the end of each trace is the peak velocity in centimeters/second for the strong-motion synthetics and the peak displacement in microns for the teleseismic synthetics. In this example, the fault dip is  $90^\circ$  and the rupture velocity is  $0.8\beta$ . We see from the strong-motion synthetics

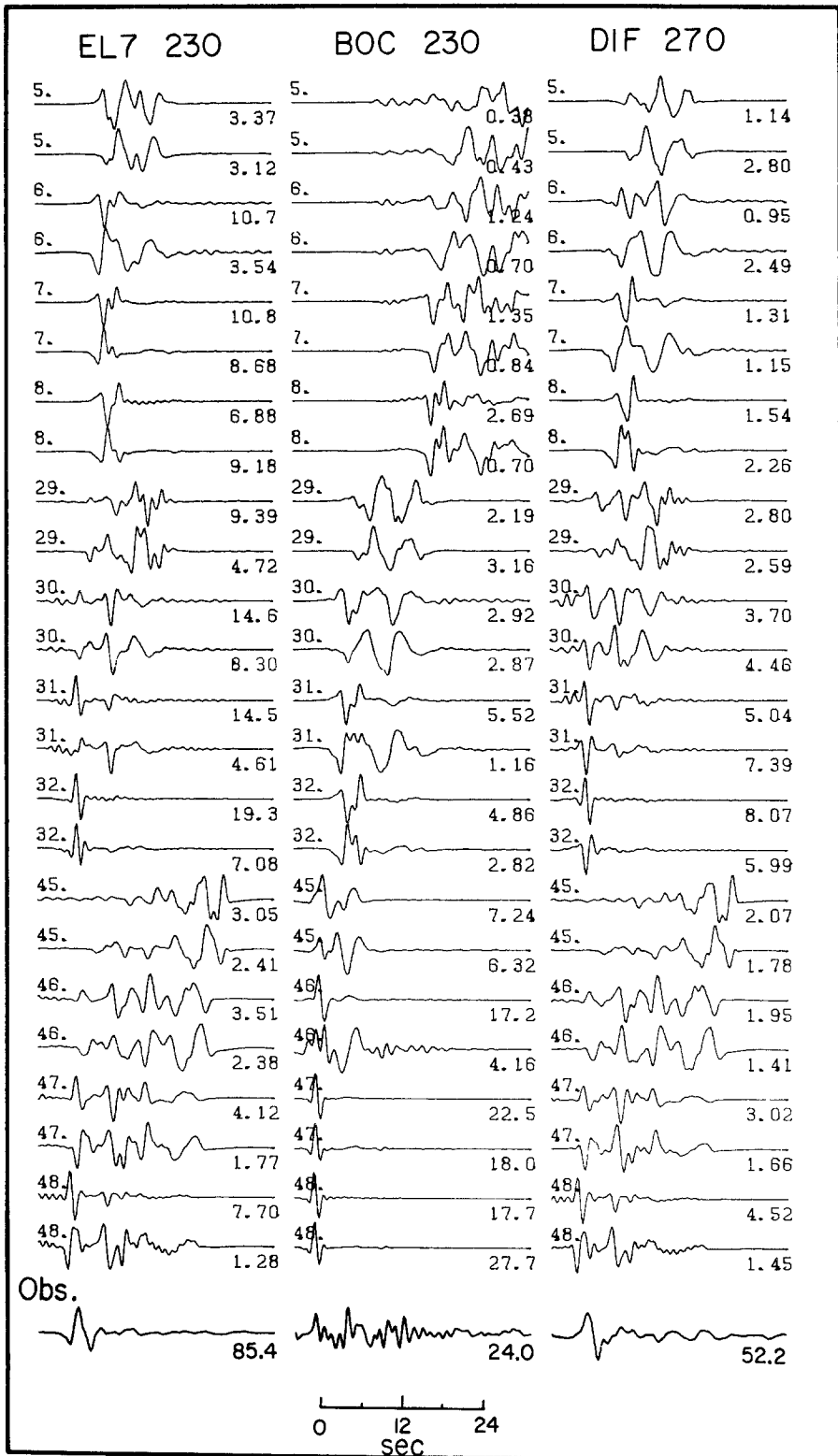


FIG. 12. Synthetics for selected subfaults for 3 of the 24 components of strong ground motion used in this study. Subfault numbers are on the left; first synthetic is for a strike-slip mechanism, second synthetic is for a dip-slip mechanism. Fault has a  $90^\circ$  dip, rupture velocity of  $0.8\beta$ , and uniform constant dislocation of 1 m. The data are shown at the bottom of the figure for comparison. Peak amplitude in centimeters/second is on the right.

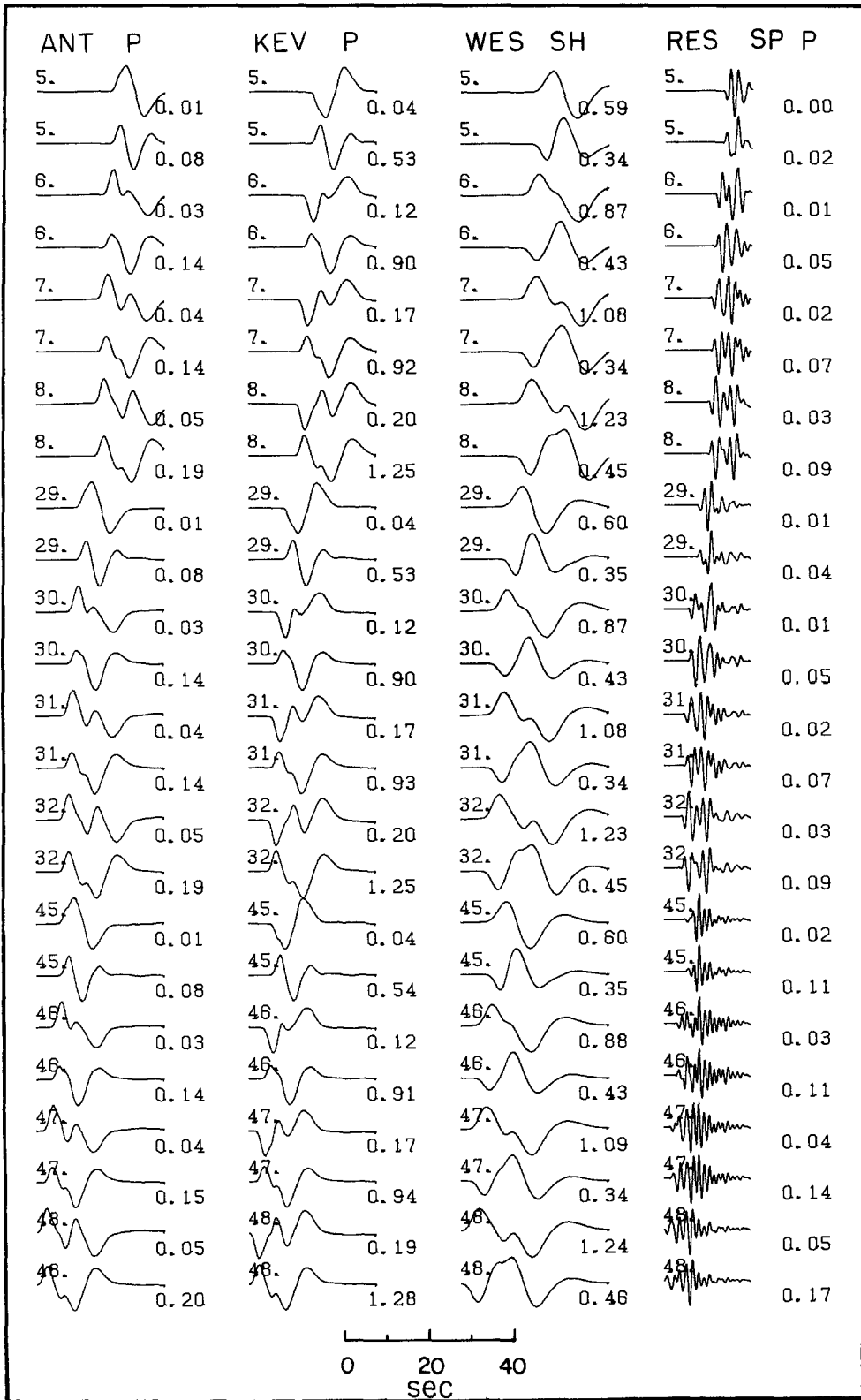


FIG. 13. Synthetics for selected subfaults for 4 of the 36 teleseismic records used in this study. Format is the same as Figure 12. Peak amplitudes given in microns.

in Figure 12 that there is significant variation in waveform both with depth and along the strike of the fault. These changes in waveform are important for resolving details on the fault. Using larger subfaults would force averaging over larger areas of the fault and some of the details would be obscured. Consider the  $230^\circ$  component of station EL7 (El Centro array station 7) shown in Figure 12. The subfault 5 synthetic is mostly direct  $S$ ; the subfault 45 synthetic is mostly Love waves. From subfaults 5 and 45, we see that surface wave energy is still arriving from the southern end of the fault long after the rupture has passed by this station. Data of this type help constrain the amount of shallow versus deep faulting. The teleseismic subfault synthetics in Figure 13 do not show the waveform variations along the length of the fault that are seen in the near-field. However, they do change significantly with depth. Two teleseismic subfault synthetics located at the same depth are distinguished from one another by their timing. This is why, as we discussed above, accurate timing of the teleseismic records is so important.

We can solve equation (2) by linear least squares, but the solution is unstable. The instability arises because  $A$  is an ill-conditioned matrix (condition number of several hundred), meaning that a small change in the data results in a large change in the solution. The problem may be stabilized by appending linear stability constraints giving

$$\begin{bmatrix} A \\ \lambda F \end{bmatrix} x \cong \begin{bmatrix} b \\ \lambda d \end{bmatrix} \quad (3)$$

where  $Fx \cong d$  is the set of linear constraints and  $\lambda$  is a scalar weight. By so doing, we sacrifice some of the fit to the data, but by adjusting  $\lambda$ , a satisfactory compromise can be obtained. The stability constraints may take several forms. We have tried three: (1) moment minimization, (2) smoothing, and (3) filtering of singular values. If  $F = I$ , the identity matrix, and  $d = 0$ , then  $\|x\| = [\sum_{i=1}^n x_i^2]^{1/2}$  is minimized while still requiring that the data be fit. Large, poorly resolved elements of  $x$  which do not contribute significantly to matching the waveforms will be forced to zero. Alternatively, if the set of equations  $Fx \cong d$  has a form such that  $x_i - x_j \cong 0$  where  $i$  and  $j$  are the indices of adjacent subfaults, then the solution is constrained to have a smoothly varying spatial distribution. Finally, we may high-pass filter the singular values of the  $A$  matrix. Assume that the singular value decomposition of  $A$  is  $USV^T$ , where  $U$  and  $V$  are orthogonal matrices,  $S$  is the diagonal matrix of singular values, and  $T$  indicates the transpose of the matrix. Then if  $F = VHV^T$  and  $d = 0$ , where  $H$  is a diagonal matrix with  $[H]_{ii} = 0$ ,  $i \leq k$  and  $= 1$ ,  $i > k$ , then the parts of the solution corresponding to small singular values are minimized. This approach has been used by Olson and Apsel (1982). Actually, all three of the above stabilization techniques yield quite similar results. We favor the second or smoothing method. Smoothing stabilization has an obvious physical interpretation which works well with the way we have discretized the fault plane. Each subfault has a starting and stopping phase associated with it. If large variations in dislocation are allowed between adjacent subfaults, the starting and stopping phases will be large and the data will be modeled as a linear combination of these phases. Since the starting and stopping phases are an artifact of the parameterization of the problem and have nothing to do with the earthquake source, completely erroneous results may be obtained when too large a subfault is used. If only a few large subfaults are used, there is not sufficient spatial resolution of fault details. Therefore, our approach has been to divide the fault into a large number of relatively small subfaults and to then apply smoothing constraints.

In addition to the above stabilization, the solution is constrained to be nonnegative, i.e.,  $x_i \geq 0$ . Without this constraint, the dislocations on adjacent subfaults are free to change sign. Besides being physically undesirable, such a condition leads to destructive interference between subfaults and an unstable solution. The nonnegative least-squares problem is solved using routine NNLS from Lawson and Hanson (1974). The dimensions of equation (3) are generally quite large; typical runs involve an  $A$  matrix with dimensions of 9468 by 112 or 7044 by 336. The inversion of matrices of such large dimension can lead to severe computational inefficiency on computers of limited core storage capability. These large matrices are accommodated by using a sequential Householder transformation technique (Lawson and Hanson, 1974). With this method, the  $m \times n$  matrix  $A$  is sequentially upper triangularized taking  $k$  rows at a time, where  $m \geq k \geq n$ .

All the strong-motion records are normalized to a peak amplitude of 1.0 unit. Thus each record has equal weight in the inversion. Without this normalization, a least-squares inversion would fit large-amplitude records very well and tend to ignore smaller amplitude records. Such a scheme can give biased results when trying to invert for a three-dimensional slip pattern where good station coverage is important. Runs have also been made without this normalization and the results are very similar. The teleseismic, long-period  $P$  waves are normalized to a peak amplitude of 0.5 units. The teleseismic records have large amplitudes over their entire length, while the strong-motion records have low amplitudes for a large portion of their length. Since we are using a point-by-point inversion, it is necessary to use a smaller normalization on the teleseismic records so that they will have the same total weight as the strong-motion records. As we have mentioned, the timing of the teleseismic records is crucial. It is not possible to obtain as accurate  $S$  arrival times as we did for the  $P$  waves. Without good timing the  $SH$  waveforms could introduce erroneous time shifts in the inversion. The  $SH$  waves have therefore been multiplied by 0.01 in the inversion. Even so, the  $SH$  waveforms are fit well, indicating that they are consistent with the models derived from the  $P$  waves. Considerable difficulty arose in modeling the short-period  $P$  waves. Therefore, on many of our later runs, the short-period records were multiplied by 0.01.

### INVERSION RESULTS

Our basic philosophy has been to run many different inversions, not just one or two. We have varied the type and number of records in the inversion, the type and amount of stabilization/smoothing, and the weighting of records. Over 30 separate inversions have been investigated. Table 3 lists the more noteworthy. The quantity  $\|b - Ax\|$  is the euclidean norm of the misfit between the data and the synthetics. This number can be used to compare different runs having the same input data, i.e., strong-motion records alone or teleseismic records alone, etc. The primary fault parameters we have varied are the fault dip and the rupture velocity. The rake is free to vary from pure right-lateral strike-slip to pure dip-slip (east-side down) as a function of position on the fault in each inversion. The strike is fixed at N143°W, which is the average trend of the surface trace of the Imperial fault. Inversions are initially run with the rupture velocity constrained to be a constant fraction of the local shear-wave velocity. This constraint is then relaxed and the rupture velocity is allowed to vary within set limits.

Figure 14 is the first of several figures with similar formats. Each frame in Figure 14 shows contours of dislocation in centimeters on the Imperial fault plane. The area covered is the same as the base map in Figure 10. Although the dislocation is

TABLE 3  
SUMMARY OF INVERSION RUNS

Model No	Dip (°)	Rupture Velocity	Moment $\times 10^{26}$ (dyne-cm)	$\ b - Ax\ $	Type
27	90	$0.85\beta$	5.6	13.20	Strong motion
18	80	$0.9\beta$	5.5	13.99	Strong motion
19	80	$0.85\beta$	5.7	13.71	Strong motion
14	80	$0.8\beta$	7.3	13.37	Strong motion
21	80	$0.7\beta$	9.1	14.10	Strong motion
34	90	$0.9\beta$	3.9	15.85	Teleseismic
25	90	$0.85\beta$	3.9	15.90	Teleseismic
33	90	$0.7\beta$	4.1	16.07	Teleseismic
26	80	$0.85\beta$	2.9	17.19	Teleseismic
30	90	$0.85\beta$	4.7	15.88	Strong motion and teleseismic
31	90	$0.8\beta$	5.1	15.76	Strong motion and teleseismic
32	80	$0.8\beta$	4.1	16.47	Strong motion and teleseismic
W1	90	$0.75\beta, 0.8\beta, 0.85\beta$	4.9	15.02	Strong motion and teleseismic
W2	90	$0.85\beta, 0.85\beta + 0.5$ sec, $0.85\beta + 1.0$ sec	4.9	14.87	Strong motion and teleseismic
W3	80	$0.85\beta, 0.85\beta + 0.5$ sec, $0.85\beta + 1.0$ sec	4.0	15.96	Strong motion and teleseismic
W5	90	$0.85\beta, 0.85\beta + 0.5$ sec, $0.85\beta + 1.0$ sec	7.3	7.84	Short-period <i>P</i> only
35	90	$0.85\beta$	3.8	9.25	Short-period <i>P</i> only

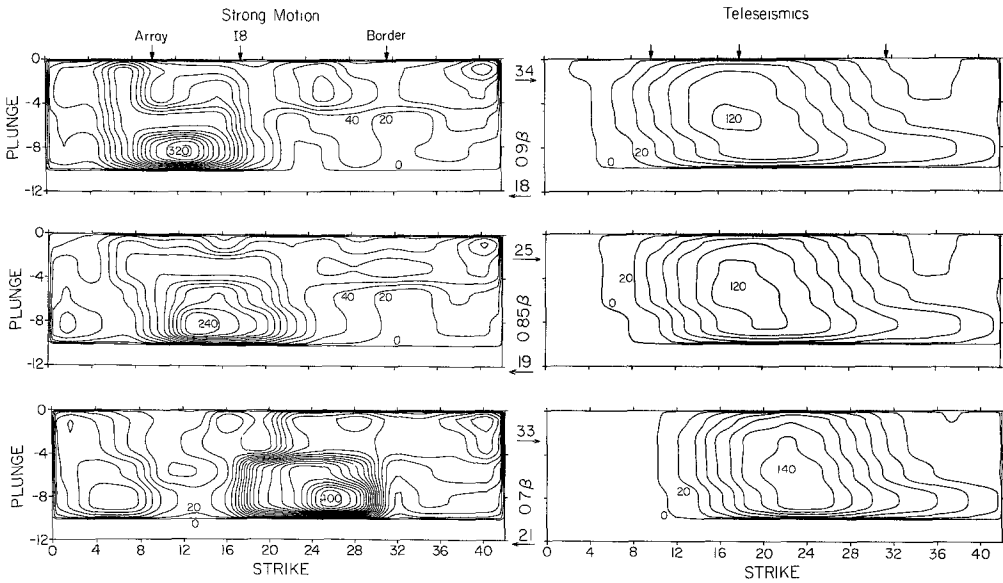


FIG. 14. Contours of dislocation in centimeters (right-lateral, strike-slip component only) on the Imperial fault plane. Figure compares inversion results using different data sets and different rupture velocities. Horizontal and vertical axes are in kilometers. Each frame of the figure covers the same area as in Figure 10. Model numbers are the same as in Table 2

constant over each subfault in the inversions, a small amount of smoothing is done in the contour plots for display purposes. Figure 14 shows how the solution changes with different constant rupture velocities. Only the strike-slip components of motion are pictured. The three frames on the left are inversions of the strong-motion data alone, and the three frames on the right are inversions of the teleseismic data alone.

The model numbers of the inversions runs are indicated in Figure 13 and in all the following figures. These numbers can be used to refer to the tabulated information in Table 3.

First consider the strong-motion solution alone. The most obvious feature is the rather localized, deep patch of larger dislocation. For the purpose of discussion, we shall refer to this feature as an asperity. There is a clear trade-off between the location of the asperity along the fault and the rupture velocity. There is also a relationship between the maximum dislocation and the assumed rupture velocity. The maximum dislocation is large for both a fast rupture ( $0.9\beta$ ) and a slow rupture ( $0.7\beta$ ), and goes through a minimum for a rupture velocity near  $0.85\beta$ . The maximum dislocation at the asperity is controlled primarily by the amplitudes of the El Centro array station records. For a high rupture velocity, the asperity is shifted northward to a point under the array, which is a near-nodal position for *SH* waves radiated to the array stations. Accordingly, the dislocation must be increased to match the observed amplitudes. For a low rupture velocity, the asperity is at a greater distance from the array and the dislocation must also be increased.

The teleseismic inversions on the right side of Figure 14 do not show as much detail as the strong-motion solutions, but they do have the same general character. The dislocation is small in the hypocentral region, grows to a maximum under Interstate 8, and then decays past the array stations. The position of the maximum dislocation is much less sensitive to the rupture velocity. This observation can be used to great advantage in simultaneous inversion. The teleseismic records constrain the timing or position of gross features on the fault while the strong-motion records resolve more of the details. The maximum dislocations for the teleseismic inversions are significantly less than the strong-motion solutions; however, they cover a broader area and the moments are similar. From Table 3, the moment estimate from the strong-motion inversions is about  $5.7 \times 10^{25}$  dyne-cm, while the moment from the teleseismic inversions is about  $4.0 \times 10^{25}$  dyne-cm. Heaton (1982) observed the same trend for the San Fernando earthquake. He obtained a slightly larger estimate of the moment from strong-motion data than from teleseismic body waves.

Figure 15 compares inversions of different data sets. Both the strike-slip and dip-slip parts of the solution are shown. The top two frames in Figure 15 show the inversion results using only the strong-motion data. The middle pair is an inversion of only the teleseismic data, and the bottom pair is a simultaneous inversion of the strong-motion and teleseismic data. The simultaneous inversion, model 31, is our best-fitting solution assuming a constant rupture velocity. The fault dip is  $90^\circ$ , the rupture velocity is  $0.8\beta$  ( $= 2.5$  km/sec in the basement material below 5 km), and the moment is  $5.1 \times 10^{25}$  dyne-cm (see Table 3). The dip-slip motion is much less than the strike-slip motion and is concentrated in the upper 5 km of sediments. The strike-slip motion is relatively small in the hypocentral region, drops to 20 cm or less near the border, then grows dramatically to 2 m under Interstate 8. North of the El Centro array, the dislocation drops off rapidly and is about 50 per cent strike-slip and 50 per cent dip-slip. The bottom of the fault is not well resolved in model 31 or in many of our other inversions, due to the imposed bottom boundary at 10.5 km. There is no reason why the fault could not be extended deeper except that the cost of computation is increased.

From our experimentation with different fixed-rupture velocities, we noticed that certain aspects of the strong-motion records are explained better by a rupture velocity greater than  $0.8\beta$ , while other features are explained better by a rupture velocity less than  $0.8\beta$ . To accommodate these observations, several inversions are

done where the rupture velocity is allowed to vary within set limits. This generalization is accomplished by allowing each subfault to rupture three separate times. Model W2 in Figure 16 shows the results of an inversion of this type. Rupture is allowed to occur within any of three windows:  $T_1$ ,  $T_2$ , and  $T_3$ .  $T_1$  is the part of the dislocation which occurs within 0.7 sec of the passage of a rupture front traveling at  $0.85\beta$ .  $T_2$  is the cumulative dislocation within 1.2 sec after the passage of the rupture front, and  $T_3$  is the cumulative dislocation within 1.7 sec after the passage of the rupture front. Model W2 is our preferred solution. Both the strong-motion and teleseismic records are used in this inversion. The dip of the fault plane for model W2 is  $90^\circ$  and the moment is  $4.9 \times 10^{25}$  dyne-cm (see Table 3). The time separation of 0.5 sec between  $T_1$ ,  $T_2$ , and  $T_3$  is not arbitrary. If the separation is too small, then the model will not allow sufficient latitude in the rupture velocity/time function. If the separation is too large, on the order of the period of the data, destructive interference can result between the waveforms of different time windows,

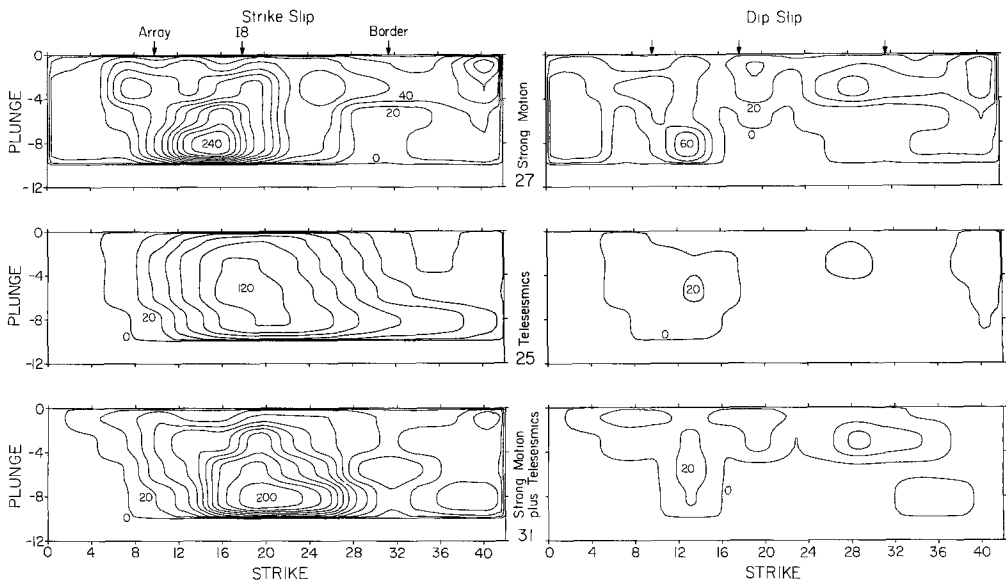


FIG 15 Contours of dislocation in centimeters on the Imperial fault plane. Figure compares strike-slip and dip-slip components for strong-motion, teleseismic, and simultaneous inversions using fixed rupture velocities. Model numbers are the same as in Table 3.

causing instability. Such instabilities can also result if the separation between windows is small, but the total number of time windows is large.

Frame  $T_3$  of model W2 is actually quite similar to model 31 (Figure 15). However, model W2 fits the strong-motion and teleseismic records significantly better. The improvement in fit is due to the fact that different sections of the fault are now allowed to rupture in time as required to explain the data. In Figure 17, the dislocations which take place in each of the three separate time windows of model W2 are plotted separately, in contrast to the cumulative plot in Figure 16. The strike-slip part of the solution is shown. We see that in moving from the fast rupture frame,  $T_1 (= 0.85\beta)$ , to the slow rupture frame,  $T_3 (= 0.85\beta + 1.0 \text{ sec})$ , the locus of maximum dislocation shifts to the south. This observation can be interpreted in one of two ways. First, the region of the fault plane near the border and 5 to 10 km north may have ruptured at a lower velocity, about  $0.7\beta$ . The asperity under

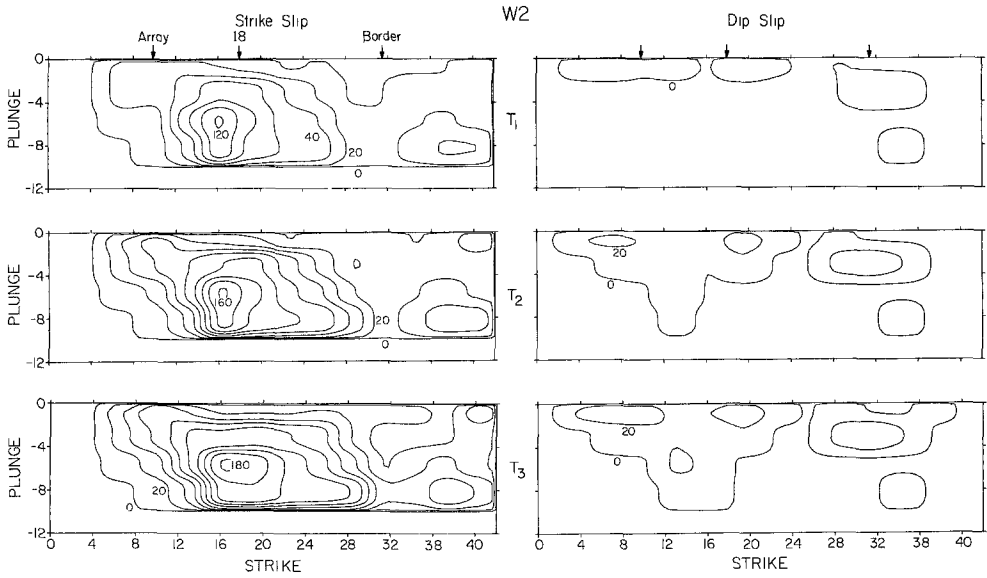


FIG. 16. Contours of dislocation in centimeters on the Imperial fault plane. Fault model has a 90° dip and three time segments:  $T_1$ ,  $T_2$ , and  $T_3$ . This model is our preferred solution. See text for details.

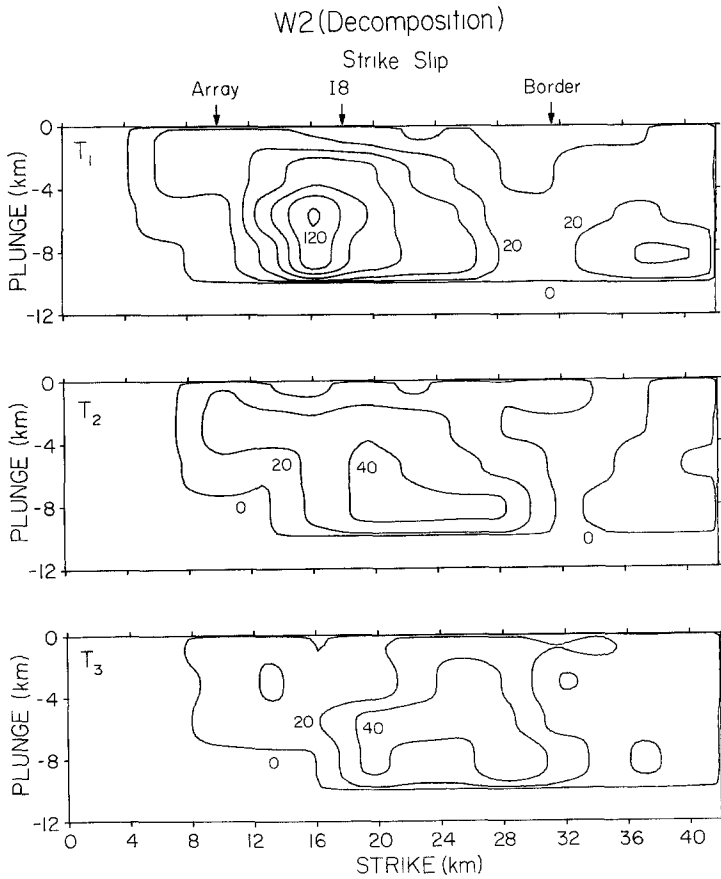


FIG. 17. Contours of dislocation in centimeters occurring in each of the three time windows of  $W_2$  (Figure 16). See text for details.

Interstate 8 ruptures at a considerably higher velocity, about  $0.9\beta$ . To preserve continuity, the rupture front must have accelerated from the border to the asperity. The second interpretation has the faulting during  $T_2$  and  $T_3$  occurring as afterslip. The entire fault may have broken with a high rupture velocity. Faulting in the region of the asperity occurs abruptly with little afterslip, whereas most of the dislocation on the fault plane south of the asperity occurs sometime after the passage of the rupture front. One may alternatively view this model as a variable rise time on the fault plane. Our analysis cannot distinguish between these two models.

The surface offsets for model W2 are generally consistent with observations of surface faulting. Observed displacements become large 5 km north of the border and extend northward for about 30 km (Sharp *et al.*, 1982). In model W2 the contours of dislocation take a sharp turn upward and increase in amplitude also about 5 km north of the border. In our model, significant surface faulting extends northward for about 25 km. The surface subfaults average over the top 2.5 km, so one should not expect the dislocations on these elements to agree in detail with the surface dislocations. It is also of interest to compare model W2 with model 9WM of Hartzell and Helmberger (1982). Model 9WM does not have the complicated timing of W2, but if we compare just the final dislocations, the two models are quite similar. Both models have relatively small amounts of faulting at the hypocenter and a minimum in slip near the border. The dislocation in the hypocentral region of 9WM is larger than in W2. However, model 9WM does not allow for a bilateral rupture and must concentrate more slip in a smaller area. Both models have an asperity under Interstate 8 with about 2 m of slip. Model 9WM has another local maximum about 5 km north of the border. In model W2, the second maximum is replaced by a broader region of large dislocation with no intervening minimum.

Evidence for the localized maximum in dislocation under Interstate 8 can be seen directly in the short-period  $P$  waves. The short-period records in Figure 8 are low amplitude for the first 6 sec. Six seconds into the records there is a clear increase in amplitudes. The hypocenter in model W2 (Figure 16) is 36 km from the northern end of the fault. Six seconds corresponds to 15 km for a rupture velocity of 2.5 km/sec ( $0.8\beta$  in the basement material), which places the rupture front at the 21 km mark in Figure 16. This position is at the beginning of the asperity. The asperity is superimposed on a much broader region of relatively large dislocation about 20 km long and entirely north of the border. The 1979 Imperial Valley earthquake appears to be actually two earthquakes; a magnitude 5 earthquake at the hypocenter south of the border, followed by a magnitude 6 earthquake north of the border.

Model W3 in Figure 18 is another simultaneous strong-motion-teleseismic, multi-time window inversion like model W2. The only difference between W2 and W3 is the dip of the fault. W3 has a dip of  $80^\circ$  to the east (W2 assumes a vertical fault plane). The major effects of introducing a nonvertical dip are to eliminate a lot of the deeper dislocation (below 8 km) and to reduce the peak dislocation from 180 to 120 cm. Model W3 fits the strong-motion records as well as W2, but does a poorer job of explaining the teleseismic records. The poorer fit to the teleseismic body waves is primarily due to the misprediction of the  $P$ -wave first motions at the near-nodal stations to the south (NNA, ANT, and ARE).

Figures 19 through 23 compare the strong-motion and teleseismic records with the synthetics for the simultaneous inversion models: W2, W3, and 31. The strong-motion data and synthetics in Figures 19 and 20 are plotted on the same vertical scales to facilitate comparison of amplitudes. The best-fitting, constant-rupture-

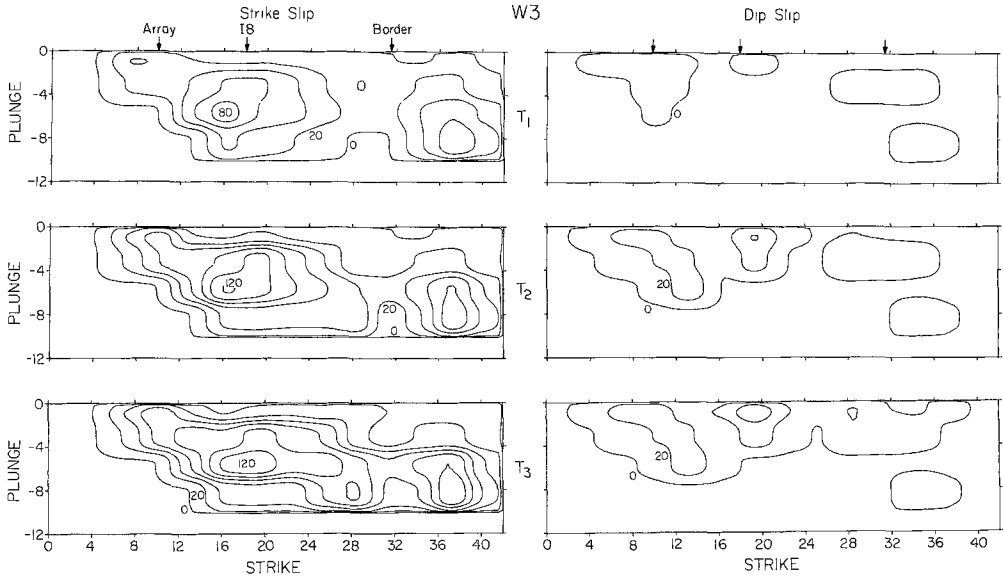


FIG. 18. Contours of dislocation in centimeters of the Imperial fault plane. Fault model has an 80° dip to the east and three time segments:  $T_1$ ,  $T_2$ , and  $T_3$ . See text for details.

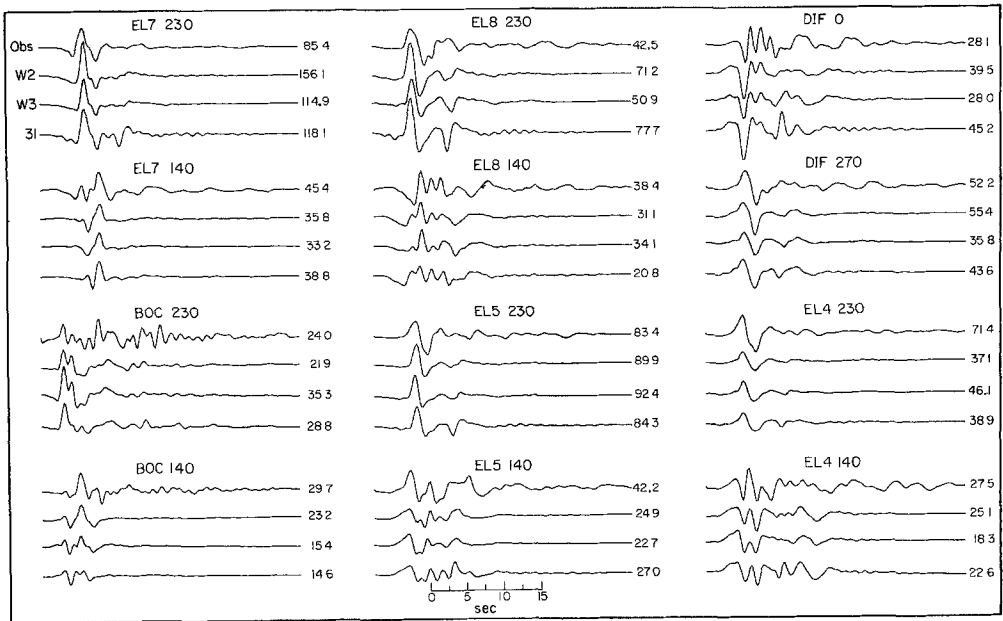


FIG. 19. Comparison between observed strong ground motion and the synthetics for three inversion models: W2, W3, and 31. The same vertical scale is used for the observations and synthetics.

velocity inversion, model 31, does a noticeably poorer job of matching the strong-motion records than W2 and W3. The more complicated timing of models W2 and W3 seems to be required by the data. The amplitudes of the long-period, teleseismic synthetics for all three models match the data fairly well (Figures 21 and 22). Although all three models W2, W3, and 31 give reasonable fits to the strong-motion

and long-period, teleseismic waveforms, model W2 provides a slightly better overall fit (Table 3). Unfortunately, none of the models match the short-period  $P$  waves (Figure 23). Stations like BLA and RES, where there is fairly good amplitude agreement, also have better waveform agreement than stations like MAT, where the amplitude of the data is much larger than the synthetics. MAT appears to be contaminated by large-amplitude arrivals which are not produced by our models. As we mentioned above, the short-period  $P$  waves have long durations which appear not to be explainable by a reasonable source model in a flat-lying, layered structure (see Figure 8). Therefore, we cannot expect to model the entire short-period record.

Figure 23 shows the synthetics for a fourth model, W5. Model W5 also results from a multi-time window inversion, but only the short-period  $P$  waves are used. The first 12.5 sec of the records are inverted in order to avoid the complications of later arrivals. The fits for model W5 are quite good; however, the source model is

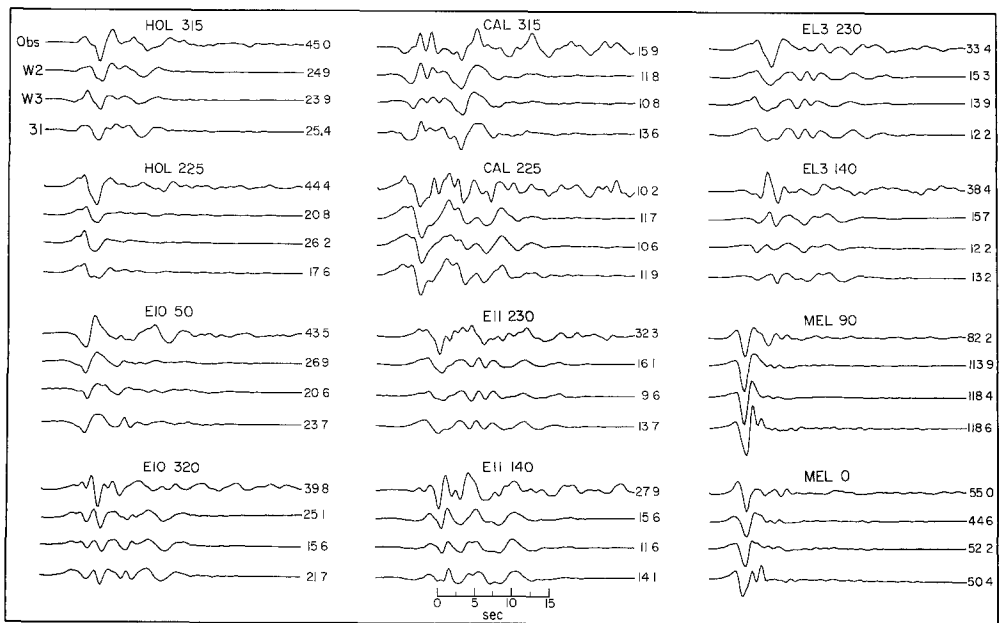


FIG. 20. Same as Figure 19

unreasonable. Figure 24 shows the contours of dislocation for model W5. The time windows  $T_1$ ,  $T_2$ , and  $T_3$  are the same as in models W2 and W3. The dip-slip part of the solution is much too large and bears no resemblance to any previous inversion. Furthermore, the synthetics for W5 are dominated by the dip-slip component of slip (compare short-period, strike-slip and dip-slip amplitudes in Figure 13). In model W5, both the strike-slip and dip-slip dislocations continue to grow to the north until they terminate at the northern end of the fault. Part of this problem may be due to the abrupt truncation of the records after 12.5 sec, necessitating a large stopping phase. Also, the separation between time windows may be too large for the short-period data, destabilizing the inversion. The strike-slip component of W5 does, however, have some similarities with model W2 (Figure 16). Both are small in the hypocentral region and both begin to increase a few kilometers north of the border. Thus, we do not consider the inversion of teleseismic short-period

records to be without hope. However, care must be exercised to obtain a stable inversion. It would be judicious to first obtain experience inverting short-period waveforms for less complicated earthquakes before tackling the intricacies seen in records of the Imperial Valley earthquake.

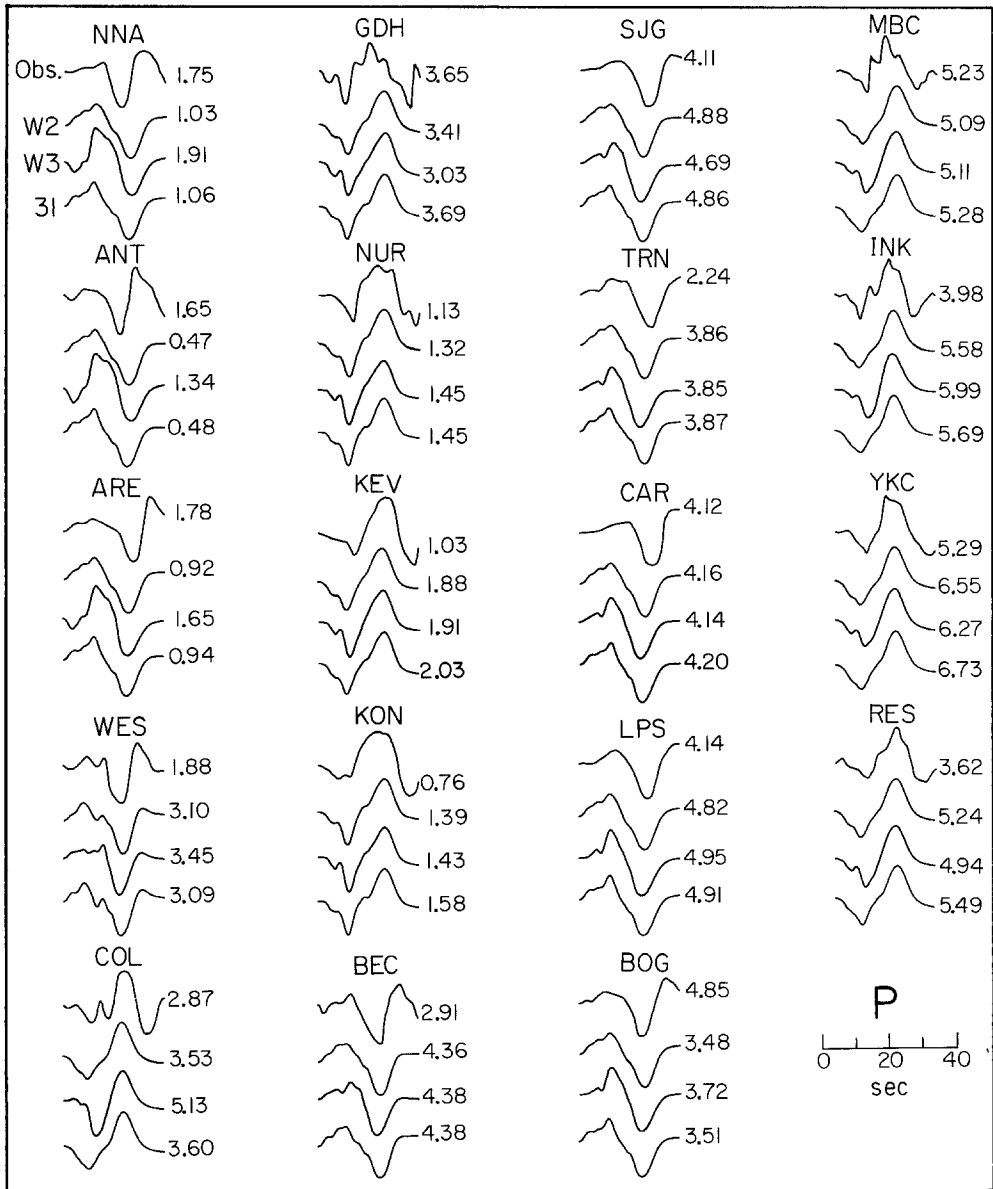


FIG. 21. Comparison between observed teleseismic, long-period, vertical  $P$  waves and the synthetics for three inversion models: W2, W3, and 31

In Figure 25, the observed and predicted peak velocities of the  $230^\circ$  component for the El Centro array stations are plotted as a function of distance from the fault. The observed amplitudes in Figure 25 are lower than those reported by Brady *et al.* (1980) because of the inversion preprocessing discussed earlier. In general, the

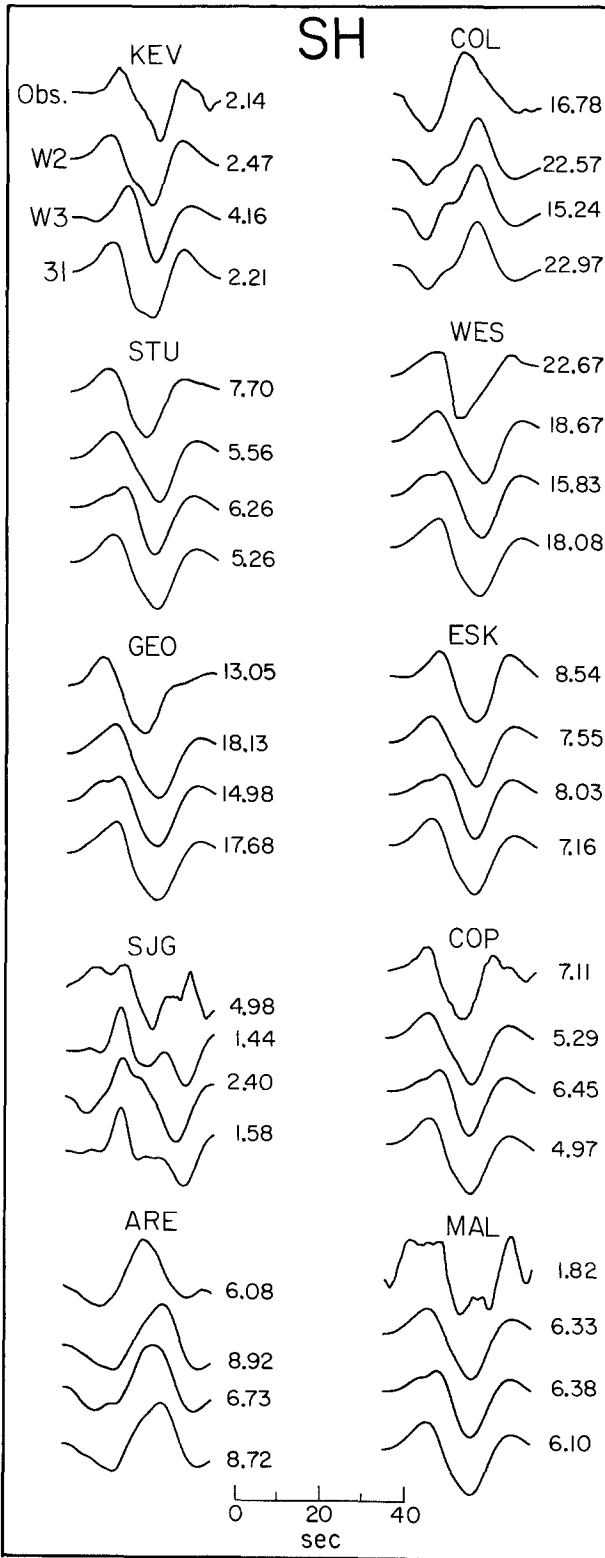


FIG. 22. Comparison between observed teleseismic, long-period, tangential SH waves and the synthetics for three inversion models W2, W3, and 31.

synthetics overestimate the velocities close to the fault and underestimate the velocities further from the fault. The large amplitude variation with distance from the fault seen in synthetic records of model W2 is caused by several effects, the most important being radiation pattern. In model W2, *SH*-wave radiation nodes occur near array stations 4 and 10 for *SH* waves produced by the asperity located

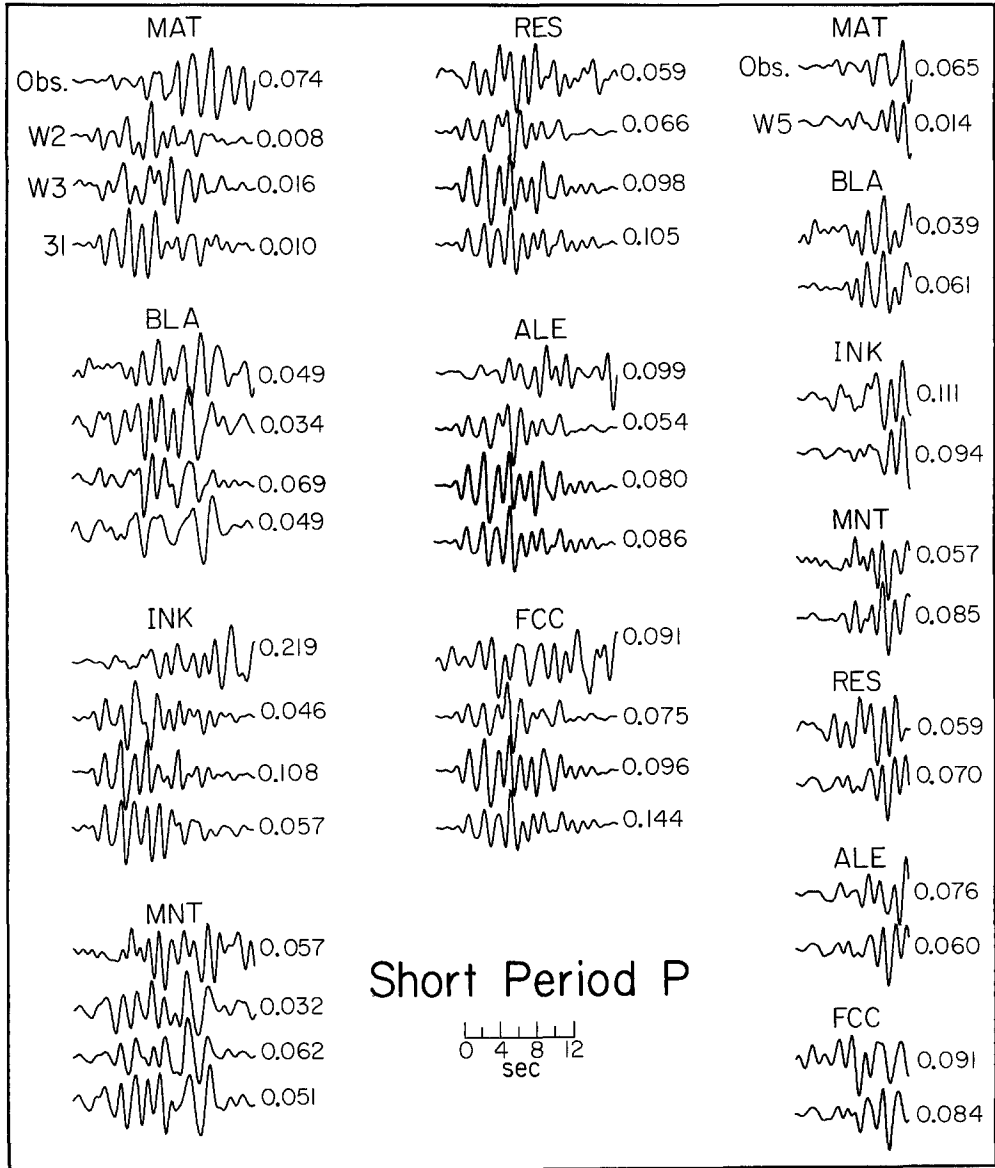


FIG. 23. Comparison between observed teleseismic, short-period, vertical *P* waves and the synthetics for four inversion models: W2, W3, 31, and W5.

beneath Interstate 8. An *SH*-wave radiation maximum occurs at array station 7, which is located directly along the strike of the asperity. The amplitude of the synthetic at array station 7 is further increased by the directivity effect due to a rupture front which traverses the asperity at a velocity very close to the local shear-wave velocity. For stations close to the fault, directivity serves to increase the

amplitude and decrease the pulse width of the direct *SH*-wave arrival. One way to decrease the variation in amplitudes for synthetics for the array stations is to move the asperity to the south. This decreases the variation across the array due to both

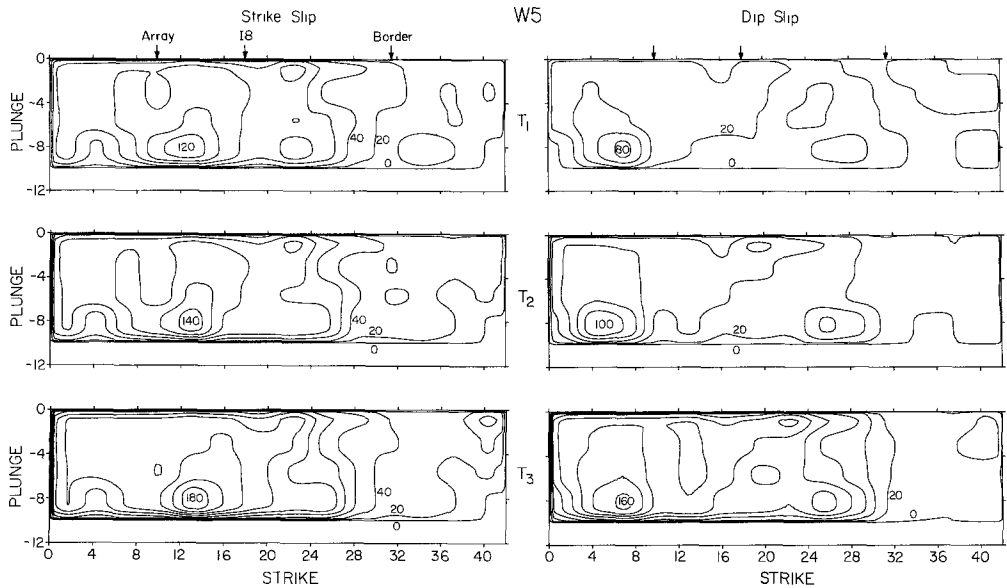


FIG. 24. Contour of dislocation in centimeters on the Imperial fault plane. Fault model has a 90° dip and three time segments.  $T_1$ ,  $T_2$ , and  $T_3$ . This solution is an unstable inversion of just the teleseismic, short-period *P* waves. See text for details.

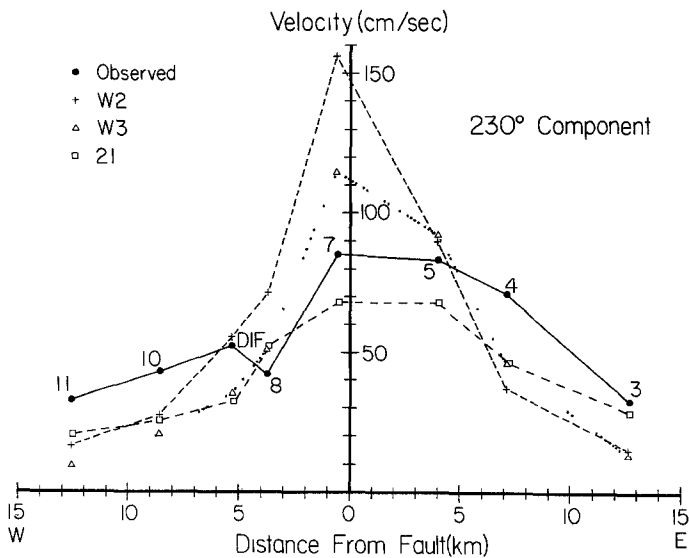


FIG. 25. Observed and predicted peak velocities as a function of distance from the surface trace of the Imperial fault for the El Centro array stations. Amplitudes are from the 230° component except station DIF which is the 270° component.

radiation pattern and directivity. Model 21, also shown in Figure 25, is a model which assumes a low rupture velocity and for which the asperity is located about 10 km south of Interstate 8 (see Figure 14). Although this model does a better job of fitting the amplitude variation seen across the array, it does a poor job of modeling

both the records of stations south of the El Centro array and the teleseismic body waves. Another alternative is to decrease the effect of radiation pattern by allowing local variations in fault strike and dip along the fault similar to those suggested by Hartzell and Helmberger (1982) and Le Bras (1983). Such variations eliminate the well-defined radiation nodes and maxima present in our simple planar models. The net effect would be to reduce amplitudes near the strike of the fault and increase them further from the fault.

After all the forward modeling done by Hartzell and Helmberger (1982) and the inversion modeling in this study, considerable insight has been gained into the kind of station distribution needed to resolve the details of rupture on a three-dimensional surface. In the case of a shallow strike-slip fault such as the Imperial fault, an array along the strike of the fault, offset from the surface trace by half the maximum fault depth, is far more diagnostic for resolving source details than an array perpendicular to the fault strike. In Figure 7 this pattern would be a succession of Bonds Corder stations parallel to the fault. Nevertheless, a great deal can be and has been learned about strong-motion wave propagation from the perpendicular-to-the-fault array.

### CONCLUSIONS

The moment of the Imperial Valley earthquake is estimated to be  $5.0 \times 10^{25}$  dyne-cm from the simultaneous inversion of local strong motions and teleseismic body waves. Teleseismic waveforms indicate a fault dip of  $90^\circ \pm 5^\circ$ . Dislocation in the hypocentral region ( $\cong 5$  km south of the border) is relatively small and drops off to 20 cm or less in the region of the border. The dislocation then increased rapidly with distance north of the border to a maximum of about 2 m under Interstate 8. Faulting dies out a short distance north of the El Centro array. Dip-slip faulting is minor compared to strike-slip and is concentrated in the sediments. The 1979 Imperial Valley earthquake appears to have initiated with a magnitude 5 earthquake at the hypocenter which then grew into, or triggered, a magnitude 6 earthquake north of the border. The best-fitting constant rupture velocity model has a rupture velocity of  $0.8\beta$  ( $= 2.5$  km/sec below 5 km). There is a suggestion of a variable rupture velocity (or variable rise time), with the rupture front accelerating from about  $0.7\beta$  near the hypocenter to  $0.9\beta$  under Interstate 8. Directivity is important for the El Centro array stations. The best-fitting simultaneous inversion model (W2) is not fundamentally different from model 9WM of Hartzell and Helmberger (1982). This study demonstrates that dislocation models can be obtained from teleseismic body waves alone that are consistent with models obtained from local strong-motion data.

### ACKNOWLEDGMENTS

This research was done at the Pasadena office of the U.S. Geological Survey. We gratefully acknowledge the cooperation and support of the faculty of the Seismological Laboratory, California Institute of Technology. We also thank Allen Olson, Ronan Le Bras, Paul Spudich, Ralph Archuleta, and Carl Johnson for helpful discussion. We thank Jim Mori for his assistance in gathering teleseismic records.

### REFERENCES

- Alekseev, A. S. and B. G. Mikhailenko (1979). Numerical modeling of transient wave fields in seismology and seismic prospecting (vertically-inhomogeneous halfspace and radially-inhomogeneous sphere), Siberian Branch—Academy of Sciences of the USSR Computing Center, Novosibirsk.
- Alekseev, A. S. and B. G. Mikhailenko (1980). The solution of dynamic problems of elastic wave propagation in inhomogeneous media by a combination of partial separation of variables and finite-

- difference models, *J. Geophys* **48**, 161-172.
- Archuleta, R. J. (1982). Analysis of near-source static and dynamic measurements from the 1979 Imperial Valley earthquake, *Bull. Seism Soc Am* **72**, 1927-1956.
- Brady, A. G., V Perez, and P. N. Mork (1980). The Imperial Valley earthquake, October 15, 1979. Digitization and processing of accelerograph records, *U S Geol Surv., Open-File Rept 80-703*
- Brune, J. N., F. L. Vernon, R. Simons, J. Prince, and E. Mena (1982). Strong-motion data recorded in Mexico during the October 15, 1979 Imperial Valley, California earthquake mainshock, in *The Imperial Valley earthquake of October 15, 1979, U.S. Geol. Surv. Profess Paper 1254*, 319-349.
- Carpenter, E. W. (1966). Absorption of elastic waves—An operator for a constant  $Q$  mechanism, Atomic Weapons Research Establishment, Report 0-4366, Her Majesty's Station Office, London, England.
- Chavez, D., J. Gonzalez, A. Reyes, M. Medina, C. Duarte, J. Brune, F. Vernon, III, R. Simons, L. Hutton, P. German, and C. Johnson (1982). Mainshock location and magnitude determination using combined U.S. and Mexican data, in the Imperial Valley, California, earthquake of October 15, 1979, *U S Geol Surv Profess Paper 1254*, 51-54.
- Fuis, G. S., W. D. Mooney, J. H. Healy, G. A. McMechan, and W. J. Lutter (1982). Crustal structure of the Imperial Valley region, in *The Imperial Valley, California, earthquake of October 15, 1979, U.S. Geol. Surv. Profess. Paper 1254*, 25-49.
- Futterman, W. I (1962). Dispersive body waves, *J Geophys Res* **67**, 5279-5291
- Hartzell, S and D V HelMBERGER (1982). Strong-motion modeling of the Imperial Valley earthquake of 1979, *Bull Seism Soc Am* **72**, 571-596.
- Heaton, T H. (1982) The 1971 San Fernando earthquake. a double event?, *Bull Seism Soc Am* **72**, 2037-2062.
- Johnson, C E. (1979) I. CEDAR—An approach to the computer automation of short-period local seismic networks II Seismotectonics of the Imperial Valley of southern California, *Ph.D. Thesis*, California Institute of Technology, Pasadena, California.
- Lawson, C. L. and R. J. Hanson (1974). *Solving Least Squares Problems*, Prentice-Hall, Inc., New Jersey.
- Le Bras, R. (1983). An inversion algorithm for strong ground motion data, application to the 1979 Imperial Valley earthquake, *Bull Seism Soc Am* **73** (in press).
- Niazi, M. (1982). Source dynamics of the 1979 Imperial Valley earthquake from near-source observations (of ground acceleration and velocity), in proceedings of workshop on the dynamic characteristics of faulting inferred from recordings of strong ground motion, *U S Geol Surv., Open File Rept. 82-591*
- Olson, A H (1982). Forward simulation and linear inversion of earthquake ground motions, *Ph D Thesis*, University of California San Diego
- Olson, A. H. and R. J. Apsel (1982) Finite faults and inverse theory with applications to the 1979 Imperial Valley earthquake, *Bull Seism Soc Am* **72**, 1969-2001
- Oppenheim, A V. and R. W. Schafer (1975). *Digital Signal Processing*, Prentice-Hall, Inc., New Jersey.
- Sharp, R. V., J. J. Lienhaemper, M. G. Bonilla, D. B. Burke, B. F. Cox, D. G. Herd, D. M. Tiller, D. M. Morton, D. J. Ponti, M. J. Rymer, J. C. Tinsley, J. C. Yount, J. E. Kahle, E. W. Hart, and K. E. Sieh (1982). Surface faulting in the central Imperial Valley, in *The Imperial Valley, California, earthquake of October 15, 1979, U S Geol Surv Profess Paper 1254*, 119-143
- Spudich, P. and E. Cranswick (1982) Use of near-source seismic-array data to reveal details of the earthquake rupture process, *Earthquake Notes* **53**, 39.
- Trifunac, M. D (1971) Zero base-line correction of strong motion accelerograms, *Bull Seism Soc Am* **61**, 1201-1211
- Trifunac, M. D (1974). A three-dimensional dislocation model for the San Fernando, California, earthquake of February 9, 1971, *Bull. Seism Soc Am* **64**, 149-172.
- Trifunac, M. D., F E UdWADIA, and A. G. Brady (1973). Analysis of errors in digitized strong-motion accelerograms, *Bull Seism Soc Am* **63**, 157-187.

U S GEOLOGICAL SURVEY  
 345 MIDDLEFIELD ROAD  
 MENLO PARK, CALIFORNIA 94025 (S.H.H.)

U S. GEOLOGICAL SURVEY  
 CALIFORNIA INSTITUTE OF TECHNOLOGY  
 PASADENA, CALIFORNIA 91125 (T.H.H.)

Manuscript received 17 March 1983